

---

# PHYSICS-INFORMED NEURAL NETWORK ESTIMATION OF MATERIAL PROPERTIES IN SOFT TISSUE NONLINEAR BIOMECHANICAL MODELS

---

A PREPRINT

✉ **Federica Caforio**<sup>\*1,2,3</sup>, ✉ **Francesco Regazzoni**<sup>4</sup>, ✉ **Stefano Pagani**<sup>4</sup>, ✉ **Elias Karabelas**<sup>1,3</sup>, ✉ **Christoph Augustin**<sup>2,3</sup>, ✉ **Gundolf Haase**<sup>1,3</sup>, ✉ **Gernot Plank**<sup>2,3</sup>, and ✉ **Alfio Quarteroni**<sup>†4,5</sup>

<sup>1</sup>Department of Mathematics & Scientific Computing, NAWI Graz, University of Graz, Austria

<sup>2</sup>Gottfried Schatz Research Center: Division of Biophysics, Medical University of Graz, Austria

<sup>3</sup>BioTechMed-Graz, Austria

<sup>4</sup>MOX, Department of Mathematics, Politecnico di Milano, Italy

<sup>5</sup>Institute of Mathematics, EPFL, Switzerland

December 21, 2023

## ABSTRACT

The development of biophysical models for clinical applications is rapidly advancing in the research community, thanks to their predictive nature and their ability to assist the interpretation of clinical data. However, high-resolution and accurate multi-physics computational models are computationally expensive and their personalisation involves fine calibration of a large number of parameters, which may be space-dependent, challenging their clinical translation. In this work, we propose a new approach, which relies on the combination of physics-informed neural networks (PINNs) with three-dimensional soft tissue nonlinear biomechanical models, capable of reconstructing displacement fields and estimating heterogeneous patient-specific biophysical properties. The proposed learning algorithm encodes information from a limited amount of displacement and, in some cases, strain data, that can be routinely acquired in the clinical setting, and combines it with the physics of the problem, represented by a mathematical model based on partial differential equations, to regularise the problem and improve its convergence properties. Several benchmarks are presented to show the accuracy and robustness of the proposed method and its great potential to enable the robust and effective identification of patient-specific, heterogeneous physical properties, e.g. tissue stiffness properties. In particular, we demonstrate the capability of the PINN to detect the presence, location and severity of scar tissue, which is beneficial to develop personalised simulation models for disease diagnosis, especially for cardiac applications.

**Keywords** nonlinear biomechanics · parameter estimation · physics-informed neural networks

## 1 Introduction

Delivering diagnoses and treatments that are specific and optimised for each patient is the aim of precision medicine. Despite impressive advances in diagnostic and therapeutic modalities, the development of personalised therapies and outcomes aimed at improving the efficacy and safety of treatments is still a challenging effort. The synergy of biomedical imaging and computational modeling enabled significant progress in this direction [1, 2]. However, major challenges related to the development of efficient mathematical models and methods need to be addressed to attain the translation of computational modeling into a clinically useful modality. In particular, modeling must move from a universal perspective investigating generic physiological and pathological mechanisms towards a personalised

---

\*Corresponding author, federica.caforio@uni-graz.at

†Professor Emeritus

approach, to quantitatively evaluate the patient’s physiology and enable patient-specific diagnoses and predictions on the impact of a therapeutic choice on the clinical outcome [3]. An established research direction to solve the related inverse problems, i.e. to estimate case-specific model parameters and biomarkers using available measurements relies on the use of data assimilation techniques [4]. These are either based on variational or stochastic approaches [5, 6] and have shown promising results, f.e. in cardiovascular models [7–12]. However, these methods require numerous evaluations of the expensive forward problem, compromising overall efficiency. The exponentially growing field of machine learning enables alternative strategies [13], which require rich and sufficient data to learn a reliable surrogate model of the phenomenon considered at a reduced computational complexity and cost. However, in the context of biophysical applications, the cost of data acquisition can be prohibitive and impractical. Consequently, the use of pure data-driven (black-box) function approximations may not be appropriate. Recently, there has been a growing interest in novel approaches integrating data-driven and physics-based knowledge. An approach based on hyperelastic physics-augmented neural networks [14] has been recently proposed, which aims at reconstructing constitutive models with neural networks (NN) fulfilling all important mechanical constraints of hyperelasticity and are calibrated to (strain and stress) data generated with an analytical potential. Note that these approaches are embedded in a Finite Element Method (FEM) framework, i.e. they aim at substituting analytical constitutive models in FEM simulations in mechanics. Similarly, in [15] a physics-informed machine-learning methodology is proposed to learn generic constitutive laws of soft tissues using stress-strain data, whereas in [16] the authors propose a methodology integrating deep neural networks and FEM for solving forward and inverse problems in nonlinear biomechanics. Another approach is represented by physics-informed neural networks (PINNs) [17, 18], i.e. neural network algorithms integrating information from the physical knowledge of the problem, which is represented by a mathematical model based on partial differential equations (PDEs). In order to enforce the network output to fulfill the PDE equations and the initial and boundary conditions, the residuals of the physical equations are specifically encoded into the loss function of the neural network as constraints. This complementary information acts as a regularisation constraining the space of admissible solutions (weights and biases of the network) to a tractable size. Therefore, the convergence and robustness properties of the method are drastically improved with respect to standard black-box machine learning strategies, especially for scarce data. In addition, since partial derivatives can be calculated with automatic differentiation (AD) [19], PINNs are mesh-free methods. As a result, it is possible to train PINNs effectively by evaluating residuals of PDEs at random locations in the space-time domain. To date, such models have been employed to solve dynamical problems involving PDEs, e.g. in fluid dynamics [20, 21], linear elasticity [22], electrophysiology [23–25] and molecular transport [26]. First efforts have been made in [27, 28] to perform parameter estimation in linear elasticity in 2D and in [29] to generate fast surrogate models of cardiac biomechanics based on the integration of shape models and PINNs. However, to the best of the authors’ knowledge, this approach has not yet been extended for solving inverse problems arising in soft tissue nonlinear biomechanical modelling, and in particular for cardiac applications. In this work, we present a novel methodology based on PINNs to accurately estimate patient-specific parameters in three-dimensional soft tissue nonlinear biomechanical models [30], with a particular interest in cardiac applications. We extend the vanilla approach, first proposed in [17], to solve the inverse problem arising in soft tissue nonlinear biomechanics, when the tissue properties are not known *a priori* and may be space-dependent. In most cases, scarce data are available in practical clinical applications, f.e. displacement and strain information retrieved from CINE-MRI or tagged-MRI images, and there is no information on stresses. The suggested approach enables the estimation of space-dependent parameters using only a limited set of displacement and, in certain instances, strain data, dispensing from using stress data. The predicted outcomes align with high-resolution finite element simulations in various test cases representing both healthy and pathological conditions. Furthermore, we demonstrate the robustness of model inference in the presence of noise, and we evaluate diverse configurations of the neural network, investigating how training data and neural network architecture influence the precision and accuracy of predictions. The rest of the manuscript is structured as follows: Section 2 is devoted to the description of the inverse problem strategy based on PINNs for estimating constant and space-dependent parameters in soft tissue nonlinear biomechanical models; Section 3 includes numerous test cases where we show the performance of the methodology with different degree of complexity in terms of the constitutive law of the tissue and heterogeneity of the parameters to be estimated, and we study the influence of varying the number of observation and collocation points as well as level of noise on the accuracy of the inferred results; in Section 4 we discuss the properties and future perspectives of the methodology; Section 5 includes final comments on this work.

## 2 Methods

### 2.1 Parameter Estimation with PINNs

In this work, we present a novel approach based on the use of PINNs to estimate constant and space-dependent model parameters in soft tissue biomechanics.

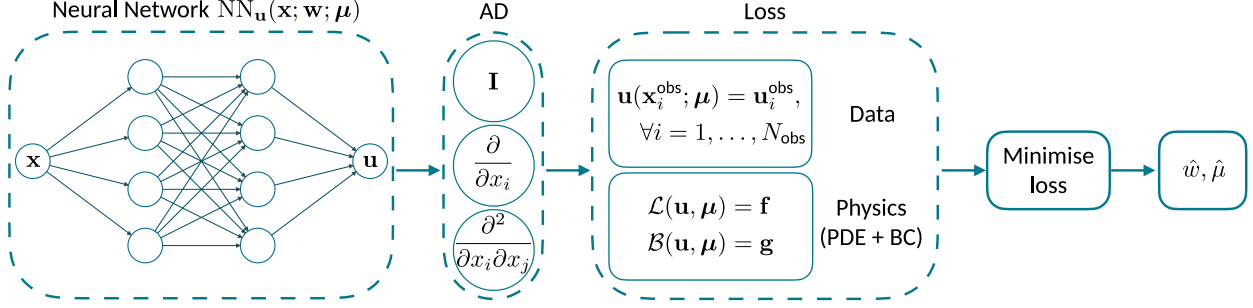


Figure 1: Schematic of PINNs. Left: A standard fully-connected neural network parameterised by biases and weights  $\mathbf{w}$  to approximate a function  $\mathbf{u}(\mathbf{x}, \boldsymbol{\mu})$ . The set of model parameters to estimate is given by  $\boldsymbol{\mu}$ . Centre: automatic differentiation (AD) is performed to efficiently compute the derivatives involved in the differential operator  $\mathcal{L}(\mathbf{u})$  and the boundary operator  $\mathcal{B}(\mathbf{u})$  on random points. The loss function is computed, composed by the data mismatch on given observation points and the PDE and BC residuals. Minimising the loss with respect to the network parameters  $\mathbf{w}$  and the solution parameter  $\boldsymbol{\mu}$  produces the PINN  $\text{NN}_{\mathbf{u}}$ .

### 2.1.1 PINNs - a quick review

The PINN framework relies on the approximation of the parameter-to-solution map encoding the underlying physical law governing a given data set. In particular, training the network is equivalent to minimising a well-designed cost function including the residuals of the governing PDE, the initial and boundary conditions, in addition to the data discrepancy term, as depicted in Fig.1. We can express the problem to solve with the neural network as follows:

Let  $\Omega \subset \mathbb{R}^n$ ,  $n \in \mathbb{N}$  be a bounded, regular domain. Find the solution  $\mathbf{u}(\mathbf{x}; \boldsymbol{\mu}) \in \Omega$  and the unknown parameters  $\boldsymbol{\mu} \in \mathbb{R}^m$ ,  $m \in \mathbb{N}$ , of the problem:

$$\begin{cases} \mathcal{L}(\mathbf{u}; \boldsymbol{\mu}) = \mathbf{f} & \text{in } \Omega \\ \mathcal{B}(\mathbf{u}; \boldsymbol{\mu}) = \mathbf{g} & \text{on } \partial\Omega, \end{cases} \quad (1)$$

with  $\mathcal{L} : V \times \mathbb{R}^m \rightarrow V'$ ,  $\mathcal{B} : W \times \mathbb{R}^m \rightarrow W'$  differential operators,  $V$  and  $W$  suitable function spaces on  $\Omega$  (depending on the type of boundary condition considered) and  $V'$  and  $W'$  denoting their duals, given  $\mathbf{f}$  and  $\mathbf{g}$  sufficiently regular, and given  $N_{\text{obs}}$  noisy observations  $\mathbf{u}_i^{\text{obs}} = \mathbf{u}(\mathbf{x}_i^{\text{obs}}; \boldsymbol{\mu}) + \epsilon$  on the measurements points

$$\mathbf{x}_i^{\text{obs}}, \text{ for } i = 1, \dots, N_{\text{obs}}.$$

For the sake of simplicity, in this section, we consider Dirichlet Boundary conditions (BC) on the domain boundary  $\partial\Omega$  to describe the method, but this can also be extended to other types of boundary conditions (typically, Neumann and Robin BC), which are more commonly used in soft tissue mechanics and, in particular, in cardiac modelling [31], as we will show in Section 3. Then, the second condition in Equation (1) reads:

$$\mathbf{u} = \mathbf{u}_{\Gamma} \quad \text{on } \partial\Omega.$$

The neural network is trained based on the fit with the measurements and penalising the PDE and BC residual on a finite set of residual points. The number and locations of these latter points at which the equations are penalised are in our full control, whereas the observation data are available at the measurement points.

### 2.1.2 Homogeneous case

First, we consider the case of homogeneous parameters  $\boldsymbol{\mu}$  in the domain, which can then be treated as constants. The resulting problem can be considered as the following optimisation problem:

Find the weights and biases  $\mathbf{w}$  of an artificial neural network  $\text{NN}_{\mathbf{u}}$  and the unknown parameters  $\boldsymbol{\mu}$  s.t. :

$$\min_{\boldsymbol{\mu}, \mathbf{w}} (\mathcal{J}_{\text{OBS}}(\mathbf{w}) + \mathcal{J}_{\text{PDE}}(\boldsymbol{\mu}, \mathbf{w}) + \mathcal{J}_{\text{BC}}(\mathbf{w}) + \mathcal{R}(\mathbf{w})), \quad (2)$$

where the mean squared error loss functions  $\mathcal{J}_*$  and regularisation term  $\mathcal{R}(\mathbf{w})$  read, respectively:

$$\begin{aligned}\mathcal{J}_{\text{OBS}}(\mathbf{w}) &= \frac{1}{N_{\text{obs}}} \sum_{i=1}^{N_{\text{obs}}} \|\mathbf{u}_i^{\text{obs}} - \text{NN}_{\mathbf{u}}(\mathbf{x}_i^{\text{obs}}; \mathbf{w})\|^2, \\ \mathcal{J}_{\text{PDE}}(\boldsymbol{\mu}, \mathbf{w}) &= \\ &\frac{1}{N_{\text{pde}}} \sum_{i=1}^{N_{\text{pde}}} \left\| \mathbf{f}(\mathbf{x}_i^{\text{pde}}) - \mathcal{L}(\text{NN}_{\mathbf{u}}(\mathbf{x}_i^{\text{pde}}; \mathbf{w}); \boldsymbol{\mu}) \right\|^2, \\ \mathcal{J}_{\text{BC}}(\mathbf{w}) &= \frac{1}{N_{\text{bc}}} \sum_{i=1}^{N_{\text{bc}}} \|\mathbf{u}_{\Gamma}(\mathbf{x}_i^{\text{bc}}) - \text{NN}_{\mathbf{u}}(\mathbf{x}_i^{\text{bc}}; \mathbf{w})\|^2, \\ \mathcal{R}(\mathbf{w}) &= \lambda_w \|\mathbf{w}\|^2,\end{aligned}\tag{3}$$

with  $\{\mathbf{x}_i^{\text{pde}}\}_{i=1}^{N_{\text{pde}}}$ , and  $\{\mathbf{x}_i^{\text{bc}}\}_{i=1}^{N_{\text{bc}}}$  denoting the collocation points for the PDE residual loss and the BC loss, respectively.

Inputs of  $\text{NN}_{\mathbf{u}}$  are point coordinates, while outputs are displacement vectors computed at the input locations. The parameters  $\boldsymbol{\mu}$  are then computed as a by-product of the NN solution since forward and inverse problems are jointly solved using the same optimisation problem.

Here, we consider tanh activation functions to fulfil the requirement of differentiability. Following previous work [32], we consider a combination of stochastic and non-stochastic gradient descent algorithms. Here we employ the Adam optimiser of Keras [33] and the BFGS optimiser of `scipy` [34]. Equations are penalised at arbitrarily many points in a meshless approach, since derivatives are based on the AD engine of `tensorflow` [35]. We use a two-step optimisation approach. First,  $\text{NN}_{\mathbf{u}}$  is pre-trained on measurement data, i.e. only minimising  $\mathcal{J}_{\text{OBS}}(\mathbf{w})$ . Here, Adam optimiser is used for 600 iterations, followed by a BFGS optimisation step until convergence to a local minimum. Second,  $\text{NN}_{\mathbf{u}}$  is trained on Equation (2) using  $N_{\text{Adam}} = 600$  iterations of Adam, followed by  $N_{\text{BFGS}} = 4000$  to 8000 iterations of BFGS depending on the complexity of the test case.

### 2.1.3 Heterogeneous case

A more general approach consists in treating the parameters  $\boldsymbol{\mu}$  as fields  $\boldsymbol{\mu}(\mathbf{x})$ , i.e.  $\boldsymbol{\mu}: \Omega \rightarrow \mathbb{R}^m$ . To do so, we simultaneously train  $m + 1$  PINNs, one for displacement and  $m$  for the parameters. For brevity, we consider hereafter  $m = 1$ , i.e. one scalar, space-dependent parameter  $\mu(\mathbf{x})$ . Then, the minimisation problem reads:

Find the weights and biases  $\mathbf{w}_1, \mathbf{w}_2$  of two artificial neural networks  $\text{NN}_{\mathbf{u}}, \text{NN}_{\mu}$  s.t.:

$$\begin{aligned}\min_{\mathbf{w}_1, \mathbf{w}_2} & \left( \mathcal{J}_{\text{OBS}}(\mathbf{w}_1, \mathbf{w}_2) + \mathcal{J}_{\text{PDE}}(\mathbf{w}_1, \mathbf{w}_2) + \right. \\ & \left. \mathcal{J}_{\text{BC}}(\mathbf{w}_1, \mathbf{w}_2) + \min_{\boldsymbol{\mu}} \mathcal{J}_{\text{PRIOR}}(\boldsymbol{\mu}, \mathbf{w}_2) \right),\end{aligned}\tag{4}$$

where we have introduced the additional loss term

$$\mathcal{J}_{\text{PRIOR}}(\boldsymbol{\mu}) = \frac{1}{N_{\text{prior}}} \sum_{i=1}^{N_{\text{prior}}} \left| \mu^{\text{prior}} - \text{NN}_{\mu}(\mathbf{x}_i^{\text{prior}}; \mathbf{w}) \right|^2.\tag{5}$$

Here,  $\mu^{\text{prior}}$  denotes a prior that may include some *a priori* knowledge on the distribution of  $\mu$ ; for example, an initial educated guess for the average value of the parameter. Optimisation of Equation (4) is done using the following two-step procedure. First, the two NNs are simultaneously trained based on the loss  $\mathcal{J}_{\text{OBS}}(\mathbf{w})$ . Again, we employ 600 iterations of the Adam optimiser, followed by BFGS optimisation steps until convergence to a local minimum. Second, both NNs are trained based on Equation (4). This training involves an initial phase with  $N_{\text{Adam}}$  iterations using the Adam optimiser, followed by subsequent  $N_{\text{BFGS}}$  iterations of BFGS optimisation (the exact values of  $N_{\text{Adam}}$  and  $N_{\text{BFGS}}$  depend on the complexity of the test case considered).

## 2.2 Application to three-dimensional soft tissue nonlinear mechanics

Here we consider benchmarks for soft tissue nonlinear biomechanics. The governing PDE is given by the Cauchy momentum equation [36]. For the sake of simplicity, in this work we assume a quasi-static approximation for a passive hyperelastic material. The training dataset used in the observation loss of Eq. (3) is represented by *in silico* data randomly sampled from the solution of the high-fidelity FEM simulator `carpentry` [30, 37, 38]. The open-source software `carputils` is used to define input/output tasks and feature definition and extraction, e.g. definition of tagged

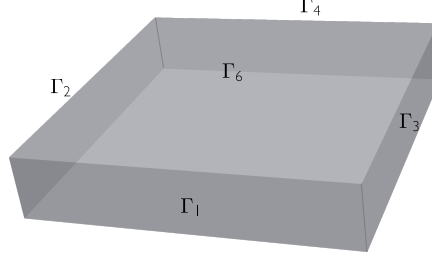


Figure 2: Problem geometry as described in Section 2.2.

regions on meshes with different parameters. The geometry of the problems studied in this work is given by the rectangular slab  $\Omega = (0, L) \times (0, W) \times (0, H)$ , with  $L = W = 10$  mm and  $H = 2$  mm. We denote the four lateral faces  $\Gamma_1 = \{0\} \times (0, W) \times (0, H)$ ,  $\Gamma_2 = (0, L) \times \{0\} \times (0, H)$ ,  $\Gamma_3 = \{L\} \times (0, W) \times (0, H)$ ,  $\Gamma_4 = (0, L) \times \{W\} \times (0, H)$ , whereas the upper and lower faces are denoted  $\Gamma_5 = (0, L) \times (0, W) \times \{0\}$  and  $\Gamma_6 = (0, L) \times (0, W) \times \{H\}$ , as depicted in Figure 2. We consider zero body forces, Neumann boundary conditions on the four lateral faces, and Robin boundary conditions on the upper and lower faces of the computational domain, respectively. The resulting problem reads:

Find  $\mathbf{u}$  s.t.:

$$\begin{aligned} -\nabla \cdot \mathbf{P}(\mathbf{u}) &= \mathbf{0} && \text{in } \Omega \\ \mathbf{P}(\mathbf{u}) \mathbf{n} &= -p J \mathbf{F}^{-\top} \mathbf{n} && \text{on } \Gamma_1 \cup \Gamma_2 \cup \Gamma_3 \cup \Gamma_4 \\ \mathbf{P}(\mathbf{u}) \mathbf{n} + k \mathbf{u} &= 0 && \text{on } \Gamma_5 \cup \Gamma_6, \end{aligned} \quad (6)$$

where  $\mathbf{P}$  denotes the first Piola-Kirchoff stress tensor,  $\mathbf{F}$  denotes the deformation tensor, and  $J = \det(\mathbf{F})$ . For a hyperelastic material  $\mathbf{P}$  can be obtained from the associated strain energy function  $\mathcal{W} = \mathcal{W}(\mathbf{F})$  as follows:

$$\mathbf{P} = \frac{\partial \mathcal{W}}{\partial \mathbf{F}}.$$

According to standard assumptions in soft tissue modelling, particularly in the cardiac setting [39], the tissue is modelled as nearly incompressible [40]. Further,  $\mathbf{n}$  denotes the unit outward normal vector on  $\{\Gamma_i\}_{i=1}^6$ . The observation data used to train the neural network (first loss term in Equation (3)) is the FEM numerical solution of the test case considered, uniformly sampled in the domain to obtain  $\mathbf{u}_i^{\text{obs}}$ , for  $i = 1, 2, \dots, N_{\text{obs}}$ . To test the robustness of the proposed approach, we mimic the presence of measurement error by corrupting these data through additive white noise, i.e. zero-mean Gaussian noise with variable standard deviation  $\sigma$ :

$$\tilde{\mathbf{u}} = \mathbf{u} + \epsilon, \quad \epsilon \sim \mathcal{N}(0, \sigma^2) \quad (7)$$

We can then compute the signal-to-noise ratio as

$$\text{SNR} = \frac{3\sigma}{\max(\mathbf{u})}.$$

The loss associated with the boundary terms for Equation (6) reads:

$$\mathcal{J}_{\text{BC}}(\mathbf{w}) =$$

$$\begin{aligned} \lambda_{\text{BC},1} \sum_{j=1}^4 \frac{1}{N_{\text{bc},j}} \sum_{i=1}^{N_{\text{bc},j}} \left\| \mathbf{P}^{ij} \mathbf{n}^j + p J^{ij} \mathbf{F}^{-\top, ij} \mathbf{n}^j \right\|^2 \\ + \lambda_{\text{BC},2} \sum_{j=5}^6 \frac{1}{N_{\text{bc},j}} \sum_{i=1}^{N_{\text{bc},j}} \left\| \mathbf{P}^{ij} \mathbf{n}^j + k \text{NN}_{\mathbf{u}}^{ij} \right\|^2, \end{aligned}$$

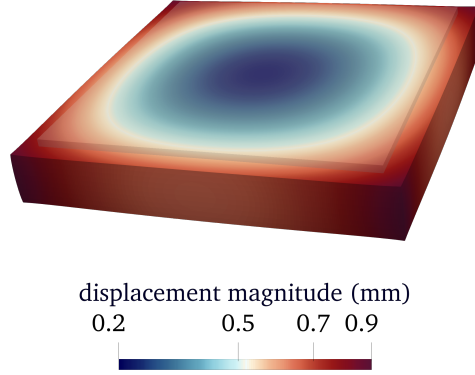


Figure 3: Isotropic test case of Section 3.1, FEM displacement magnitude in mm. The rest configuration is superposed in shaded grey to the deformed configuration.

where we introduced the shorthand notations

$$\begin{aligned} \text{NN}_{\mathbf{u}}^{ij} &:= \text{NN}_{\mathbf{u}}(\mathbf{x}_i^{\text{bc}j}; \mathbf{w}), \\ J^{ij} &:= J(\text{NN}_{\mathbf{u}}^{ij}), \\ \mathbf{F}^{-\top, ij} &:= \mathbf{F}^{-\top}(\text{NN}_{\mathbf{u}}^{ij}), \\ \mathbf{P}^{ij} &:= \mathbf{P}(\text{NN}_{\mathbf{u}}^{ij}), \end{aligned}$$

and  $\mathbf{n}^j$  denotes the outer unit normal to  $\Gamma_j$ . The architecture of  $\text{NN}_{\mathbf{u}}$  is composed by 3 hidden fully connected layers, consisting of 32, 16 and 8 neurons, respectively. The architecture of  $\text{NN}_{\mu}$  is composed by 3 hidden fully connected layers, consisting of 12, 8 and 4 neurons, respectively. In Section A.1 we include a comparison of the PINN predictions considering a common architecture for PINNs with the same number of neurons per layer [18, 20, 41, 42] to show that the proposed architecture is suitable to reach the same accuracy at a reduced computational cost.

### 3 Results

In what follows we consider hyperelastic materials of different complexity that model isotropic or anisotropic tissues with homogeneous or heterogenous biomechanical properties. We also assess the capability of the inverse problem strategy to detect and quantify scar tissue based solely on displacement and strain data in the domain.

#### 3.1 Homogeneous isotropic material

As a first test case, we consider the nearly-incompressible, isotropic Neo-Hookean material with homogeneous stiffness [36]:

$$\mathcal{W} = \frac{\mu}{2}(J^{-2/3}I_1 - 3) + \frac{\kappa}{2}(J - 1)^2, \quad (8)$$

with stiffness parameter  $\mu = 10$  kPa, bulk modulus  $\kappa = 1000$  kPa enforcing near incompressibility, and first invariant  $I_1 = \text{tr}(\mathbf{C})$ , with  $\mathbf{C} = \mathbf{F}^T \mathbf{F}$  right Cauchy-Green deformation tensor. The pressure applied at the four lateral faces (see Equation (6)) for this toy problem is  $p = -8$  kPa (i.e. traction), whereas the elastic springs applied on the upper and lower faces of the slab have stiffness  $k = 10$  kPamm<sup>-1</sup>. The rest configuration, as well as the displacement computed by FEM simulation, are shown in Figure 3.

In this example, we aim at reconstructing the displacement field and the stiffness  $\mu$  utilising a PINN. We consider an initial estimate for  $\mu = 15$  kPa, i.e. an overestimation of the ground truth by 50 %.

We additionally examine the sensitivity of the PINN predictions with respect to the number of training data. For this study we consider four settings, respectively:

Relative error on $\mu$				
SNR	Setting 1	Setting 2	Setting 3	Setting 4
0.00	2.4e-2	2.4e-2	2.9e-2	2.8e-2
0.05	0.4e-2	1.2e-2	1.4e-2	1.9e-2
0.10	1.1e-1	4.0e-2	1.1e-2	7.0e-3

Table 1: Relative error in the estimation of the stiffness  $\mu$  in Equation (8) in presence of noisy measurement data considering different numbers of observation and collocation points.

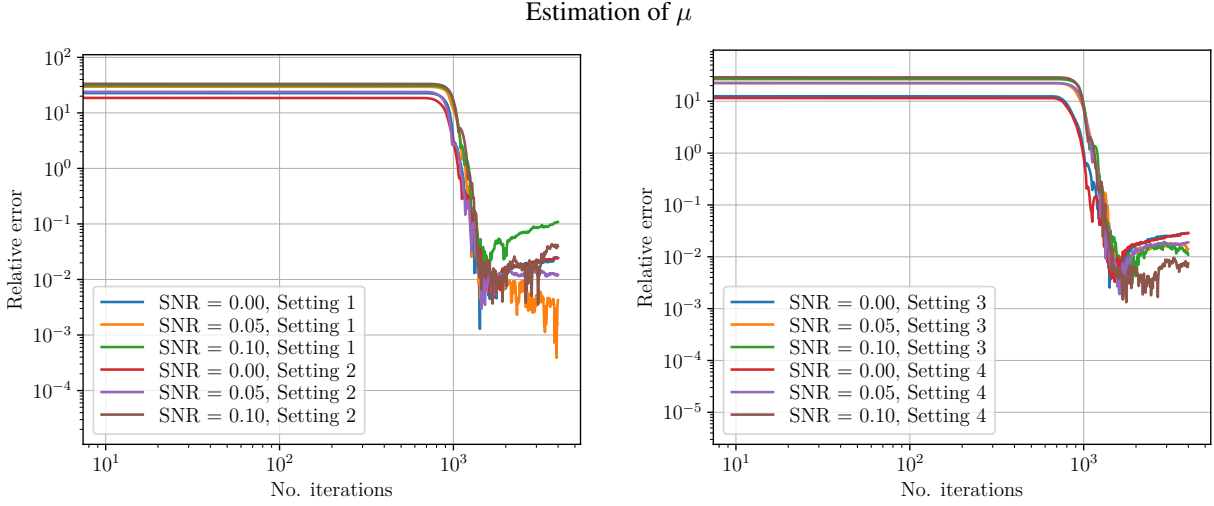


Figure 4: Isotropic material: relative estimation error of the passive stiffness  $\mu$  considering noise-free data or data corrupted by Gaussian white noise with different SNR. Result of five training processes; the solid lines depict the geometric mean, whereas the shaded region is the area spanned by the trajectories.

1.  $N_{\text{obs}} = 250$ ,  $N_{\text{pde}} = 1250$ ,  $N_{\text{bc}} = 25$  on  $\Gamma_{1,2,3,4}$ ,  $N_{\text{bc}} = 125$  on  $\Gamma_{5,6}$ ;
2.  $N_{\text{obs}} = 500$ ,  $N_{\text{pde}} = 2500$ ,  $N_{\text{bc}} = 50$  on  $\Gamma_{1,2,3,4}$ ,  $N_{\text{bc}} = 250$  on  $\Gamma_{5,6}$ ;
3.  $N_{\text{obs}} = 1000$ ,  $N_{\text{pde}} = 5000$ ,  $N_{\text{bc}} = 100$  on  $\Gamma_{1,2,3,4}$ ,  $N_{\text{bc}} = 500$  on  $\Gamma_{5,6}$ ;
4.  $N_{\text{obs}} = 2000$ ,  $N_{\text{pde}} = 10000$ ,  $N_{\text{bc}} = 200$  on  $\Gamma_{1,2,3,4}$ ,  $N_{\text{bc}} = 1000$  on  $\Gamma_{5,6}$ .

Table 1 and Figure 4 summarise the performance of the method for this test case. The algorithm shows very good robustness in the estimation of the stiffness even in presence of noise, the relative error being of the order of  $10^{-2}$  except for SNR = 10% considering the first setting, where it is one order of magnitude higher.

### 3.2 Homogeneous transverse-isotropic material

As a second example having more relevance in cardiac tissue modelling, we consider the transverse-isotropic– i.e. fibre-reinforced – nearly-incompressible Guccione material model [43]:

$$\mathcal{W} = \frac{\alpha}{2} (\exp(\bar{Q}) - 1) + \frac{\kappa}{2} (\log J)^2, \quad (9)$$

where

$$\begin{aligned} \bar{Q} := & b_f (\mathbf{f}_0 \cdot \bar{\mathbf{E}} \mathbf{f}_0)^2 + \\ & b_t \left[ (\mathbf{s}_0 \cdot \bar{\mathbf{E}} \mathbf{s}_0)^2 + (\mathbf{n}_0 \cdot \bar{\mathbf{E}} \mathbf{n}_0)^2 + 2(\mathbf{s}_0 \cdot \bar{\mathbf{E}} \mathbf{n}_0)^2 \right] + \\ & 2 b_{fs} \left[ (\mathbf{f}_0 \cdot \bar{\mathbf{E}} \mathbf{s}_0)^2 + (\mathbf{f}_0 \cdot \bar{\mathbf{E}} \mathbf{n}_0)^2 \right], \end{aligned}$$

with  $\mathbf{f}_0$  myocyte fibre orientation;  $\mathbf{s}_0$  sheet orientation;  $\mathbf{n}_0$  sheet-normal orientation. Moreover,  $\bar{\mathbf{E}} = \frac{1}{2}(\bar{\mathbf{C}} - \mathbf{I})$  denotes the isochoric Green–Lagrange strain tensor, where  $\bar{\mathbf{C}} := J^{-2/3}\mathbf{C}$ . Default values of  $b_f = 18.48$ ,  $b_t = 3.58$ , and

$b_{fs} = 1.627$  are used. The exact value of the parameter  $\alpha$ , that we want to reconstruct utilising a PINN, is 0.876 kPa. The bulk modulus  $\kappa$ , penalising compressible material behaviour, is set to  $\kappa = 1000$  kPa. The pressure applied at the four lateral faces in this toy problem (see Equation (6)) is  $p = -4$  kPa (i.e. traction), and the stiffness of the elastic springs applied on the upper and lower faces of the parallelepiped is set to  $k = 10$  kPamm $^{-1}$ . In what follows we consider two scenarios for the arrangement of the fibres. First, we set the fibre, sheet and sheet-normal orientations equal to the unit vectors  $(1, 0, 0)$ ,  $(0, 1, 0)$ ,  $(0, 0, 1)$ , respectively. The displacement computed by FEM simulation is shown in Figure 5 (left image). In the second test case, we let the fibre direction vary linearly along the  $z$ -direction from  $0^\circ$  (at  $z = 0$  mm) to  $24^\circ$  (at  $z = 2$  mm) with respect to the  $x$ -axis in the  $x$ - $y$  plane. The sheet direction varies accordingly to be orthogonal to the fibre direction in the  $x$ - $y$  plane at every location. The sheet-normal is set equal to  $(0, 0, 1)$ . The displacement computed by FEM simulation is shown in Figure 5 (right image). As a trade-off between computational cost and accuracy, we consider in both test cases  $N_{\text{obs}} = 500$  measurement points at random locations,  $N_{\text{pde}} = 2500$  residual points in  $\Omega$ ,  $N_{\text{bc}} = 50$  residual points on  $\Gamma_1, \Gamma_2, \Gamma_3, \Gamma_4$ , respectively, and  $N_{\text{bc}} = 250$  residual points on  $\Gamma_5, \Gamma_6$ . In this test case as well, we focus on the reconstruction of the displacement field and estimation of the

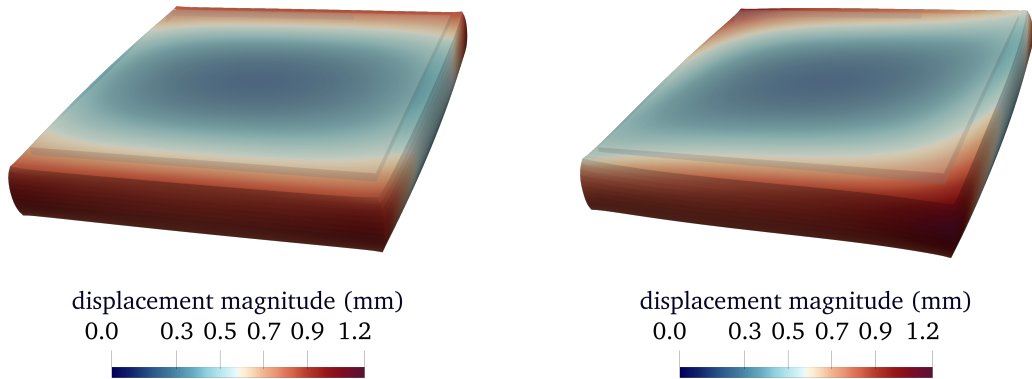


Figure 5: Transverse-isotropic test case of Section 3.2, FEM displacement magnitude in mm. Left: constant fibre orientation along  $x$ -axis. Right: varying fibre orientation ( $0^\circ$ - $24^\circ$  with respect to the  $x$ -axis in the  $x$ - $y$  plane). The rest configuration is superposed in shaded grey to the deformed configuration.

the parameter  $\alpha$  using a PINN. We consider an initial guess for  $\alpha = 1.314$  kPa, i.e. an overestimation of 50% with respect to the exact value. Table 2 and Figure 6 depict the performance of the method in this setting. The method shows a very satisfactory robustness in the estimation of the stiffness even in presence of noise, the relative error being of the order of  $10^{-2}$  also in this case.

Relative error on $\alpha$		
SNR	Constant fibre	Varying fibre
0.00	6.8e-2	7.0e-2
0.05	2.1e-2	1.9e-2
0.10	5.9e-2	4.6e-2

Table 2: Transverse-isotropic test case. Relative error on the PINN estimation of the stiffness parameter  $\alpha$  in Equation (9) in presence of noisy measurements with constant fibre orientation (along  $x$ -axis) or varying fibre orientation ( $0^\circ - 24^\circ$  with respect to the  $x$ -axis in the  $x$ - $y$ -plane)

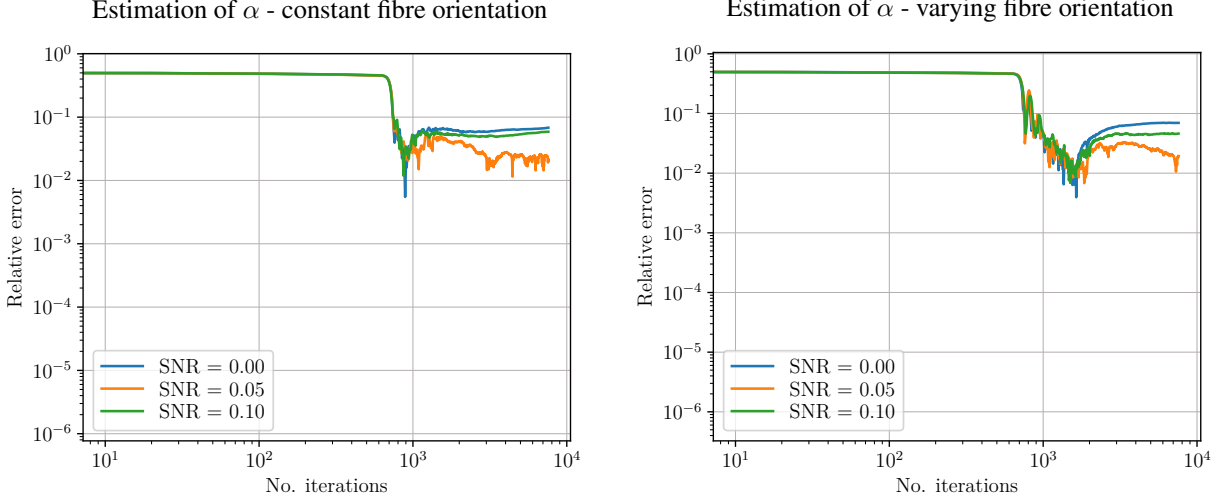


Figure 6: Transverse-isotropic material. Relative error on the estimation of the passive stiffness  $\alpha$  considering noise-free data or data corrupted by Gaussian white noise with different SNR. Results of five training processes. The solid line depicts the geometric mean; the shaded region is the area spanned by the trajectories. Results obtained considering constant fibre orientation along  $x$ -axis (left) or varying fibre orientation of  $0^\circ$  to  $24^\circ$  with respect to the  $x$ -axis in the  $x$ - $y$  plane (right).

### 3.3 Heterogeneous isotropic material

#### 3.3.1 Region-wise constant material stiffness

In this test case we consider an isotropic soft tissue, whose strain energy function is given in Equation (8), with heterogeneous stiffness. In particular, the domain is divided into two regions with different stiffness  $\mu_l = 7.5$  kPa in the left half-domain, i.e.  $x \in (0, L/2)$ , and  $\mu_r = 15$  kPa in the right half-domain, i.e.  $x \in (L/2, L)$ , with  $L = 10$  mm. The bulk modulus is set to  $\kappa = 1000$  kPa. The pressure applied at the four lateral faces (see Equation (6)) is  $p = -8$  kPa (i.e. traction), whereas the elastic springs applied on the upper and lower faces of the parallelepiped have stiffness  $k = 10$  kPamm $^{-1}$ . The rest configuration, as well as the displacement computed by means of the FEM simulation, are shown in Figure 7. For this example, we consider two possible approaches. The first one consists in reconstructing the displacement field and the stiffness coefficients  $\mu_l, \mu_r$  (both treated as a constant value in the respective subregion) by means of  $\text{NN}_{\mathbf{u}}$  as in Figure 1. The stiffness coefficients  $\mu_{\text{left}}, \mu_{\text{right}}$  are then computed as a by-product of the solution of the PINN. Here, we consider  $N_{\text{obs}} = 500$  measurement points at random locations,  $N_{\text{pde}} = 5000$  residual points in  $\Omega$ ,  $N_{\text{bc}} = 50$  residual points on  $\Gamma_1, \Gamma_2, \Gamma_3, \Gamma_4$ , respectively, and  $N_{\text{bc}} = 250$  residual points on  $\Gamma_5, \Gamma_6$ . To test the robustness of the method, we consider noisy measurements as defined in Equation (7) with SNR = 0, 0.05 and 0.1, respectively. In addition, we consider an initial guess for  $\mu_l = 15$  kPa,  $\mu_r = 25$  kPa, i.e. an overestimation of 67% with respect to their exact values. Table 3 and Figure 8 depict the performance of the

SNR	Rel. err. $\mu_l$	Rel. err. $\mu_r$	Ratio $\frac{\mu_l}{\mu_r}$
0.00	6.6e-2	0.8e-2	0.47
0.05	7.3e-2	1.6e-2	0.47
0.10	7.9e-2	5.4e-2	0.49

Table 3: Performance of the PINN in the estimation of the stiffness coefficients  $\mu_l, \mu_r$  in Equation (8) (considered as constant values in the two regions) in presence of noisy measurement data.

method in this setting. The method shows very good robustness in the estimation of both stiffness coefficients even in presence of noise. Moreover, the method very accurately estimates the ratio between the two stiffness coefficients. This information has very relevant potential for clinical applications, e.g. for scar detection. As a second approach, we consider the more general framework of the problem as given in Section 2.1.3, i.e. we consider  $\mu$  as a field  $\mu(\mathbf{x})$  (without having any geometric information on the subregions). Therefore we simultaneously train two PINNs,  $\text{NN}_{\mathbf{u}}$  and  $\text{NN}_{\mu}$ , with architectures illustrated in Section 2.2). We set in this case  $\mu^{\text{prior}} = 10$  kPa in the additional loss term in

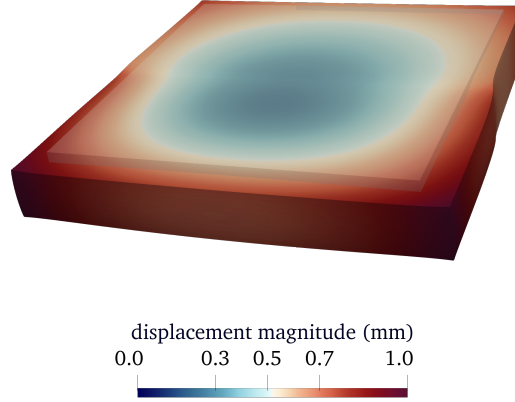


Figure 7: Isotropic test case with heterogeneous stiffness of Section 3.3.1 (two regions), FEM displacement magnitude in mm. The rest configuration is superposed in shaded grey to the deformed configuration.

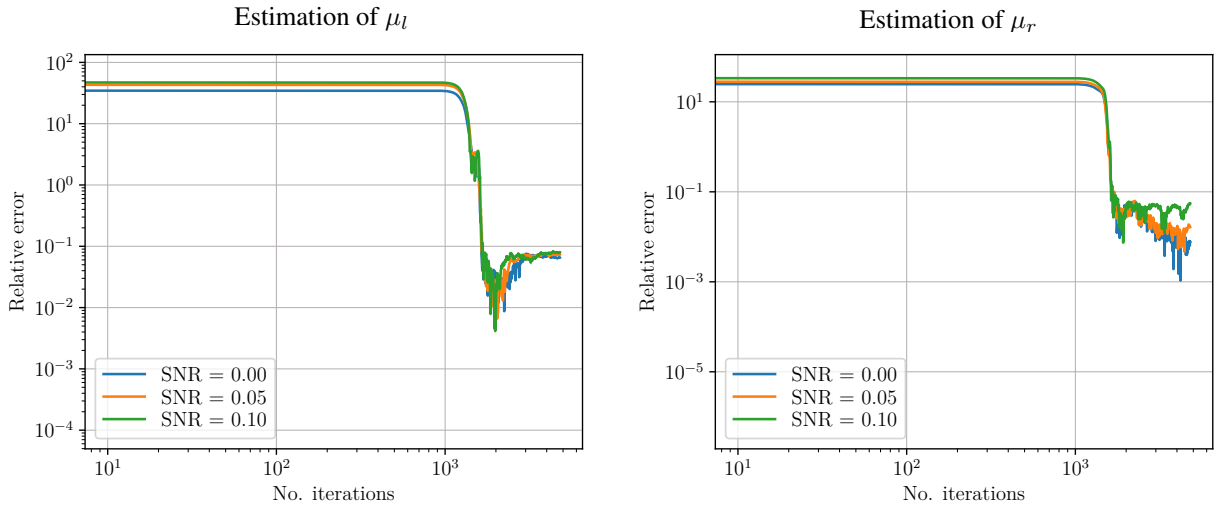


Figure 8: Isotropic heterogeneous material (two regions). Relative error on the estimation of the passive stiffness (modelled as a constant parameter in each region) considering noise-free data or data corrupted by Gaussian white noise with different SNR. Left: estimation of  $\mu_l$ . Right: Estimation of  $\mu_r$ . Results of 5 training processes. The solid line depicts the geometric mean; the shaded region is the area spanned by the trajectories.

Equation (5).  $N_{\text{Adam}}$  and  $N_{\text{BFGS}}$  are set respectively to 600 and 4000 iterations in this test case. Table 4 and Figure 9 show the  $L^2$ -relative error in the prediction of the stiffness parameter  $\mu(\mathbf{x})$  considering different levels of SNR for the observation data. For illustration purposes, we show in Figures 10 and 11 the estimated stiffness field and reconstructed displacement corresponding with one initialisation.

### 3.3.2 Internal scar inclusion

At last, we take into account a Neo-Hookean soft tissue as in Equation (8) and  $\mu_1 = 7.5$  kPa, endowed with a scar inclusion, modelled with three concentric spherical regions with centre  $(3, 3, 1)$  mm and stiffness  $\mu_2 = 15$  kPa (inner sphere with radius 1 mm),  $\mu_3 = 12.5$  kPa (spherical shell with outer radius 1.5 mm) and  $\mu_4 = 10$  kPa (spherical shell with outer radius 2 mm), respectively. The bulk modulus is set to  $\kappa = 500$  kPa. The pressure applied at the four

SNR	$L^2$ -rel. err. $\mu_l$	$L^2$ -rel. err. $\mu_r$	Ratio $\frac{\mu_{l,avg}}{\mu_{r,avg}}$
0.00	7.5e-2	6.0e-3	0.53
0.05	7.3e-2	4.0e-3	0.54
0.10	6.4e-2	2.2e-2	0.55

Table 4: Performance of the PINN in the estimation of the stiffness (modelled as a field  $\mu(\mathbf{x})$ ) in Equation (8) in presence of noisy measurement data.

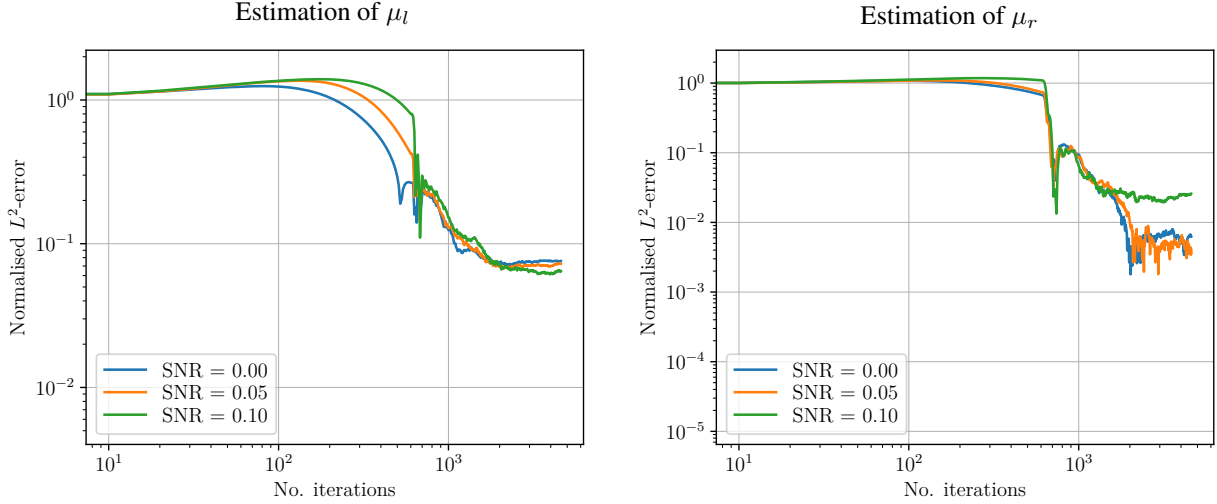


Figure 9: Isotropic heterogeneous material (two regions). Relative error on the estimation of the passive stiffness (modelled as a field  $\mu(\mathbf{x})$ ) considering noise-free data or data corrupted by Gaussian white noise with different SNR. Left: estimation of  $\mu_l$ . Right: Estimation of  $\mu_r$ . Results of five training processes. The solid line depicts the geometric mean; the shaded region is the area spanned by the trajectories.

lateral faces (see Equation (6)) is  $p = -8$  kPa (i.e. traction), whereas the elastic springs applied on the upper and lower faces of the parallelepiped have stiffness  $k = 10$  kPamm $^{-1}$ . We consider  $\mu^{\text{prior}} = 7.5$  kPa in the additional loss term in Equation (5).  $N_{\text{Adam}}$  and  $N_{\text{BFGS}}$  are set respectively to 1000 and 8000 iterations. The rest configuration of this test case, as well as the displacement computed with a FEM simulation, are shown in Figure 12 (left image). As regards the number of observation and collocation points, we consider  $N_{\text{obs}} = 1000$ ,  $N_{\text{pde}} = 5000$ ,  $N_{\text{bc}} = 100$  on  $\Gamma_{1,2,3,4}$  and  $N_{\text{bc}} = 500$  on  $\Gamma_{5,6}$ . To improve the convergence properties of the method, we also use observation data corresponding to the Green-Lagrange strain tensor to train the PINN, also retrieved from *in silico* FEM solutions (see Figure 12, right image). For illustration purposes, we depict the estimated stiffness field and the reconstructed displacement corresponding with one initialisation in case of noise-free data in Figure 13 and considering noisy data with SNR= 0.1 in Figure 14. Figure 15 (left image) shows the relative  $L^2$ -error in the estimation of the field  $\mu(\mathbf{x})$  considering different levels of SNR on the observation data. To consider a more realistic scenario, we also assume that the displacement and strain data are only available at a lower spatial resolution, i.e., instead of considering the original spatial resolution of 0.2 mm, we assume that these data are in form of digital images with pixel spacing equal to 0.4 mm. The PINN prediction stiffness field is very robust to this modification as depicted in Figure 15 (right image). Figure 16 shows the predicted stiffness field and displacement by PINNs corresponding to one initialisation in case of noise-free data, whereas Figure 17 depicts the case with noisy data (SNR= 0.1). Table 5 summarises the normalised  $L^2$ -error on  $\mu(\mathbf{x})$  in the two scenarios considered. For the sake of completeness, in Section A.1 we study the impact of the NN architecture on the accuracy of the method, whereas in Section A.2 we analyse the impact of the number of training points on the estimation of the stiffness field and reconstruction of the displacement field.

## 4 Discussion

The results in this work indicate that our PINN-based method for reconstructing stiffness properties in problems related to soft tissue nonlinear biomechanics is a promising approach, also for complex constitutive laws. In addition, our results are accurate in the presence of noise, even with a limited set of available measurement points. Our problem formulation

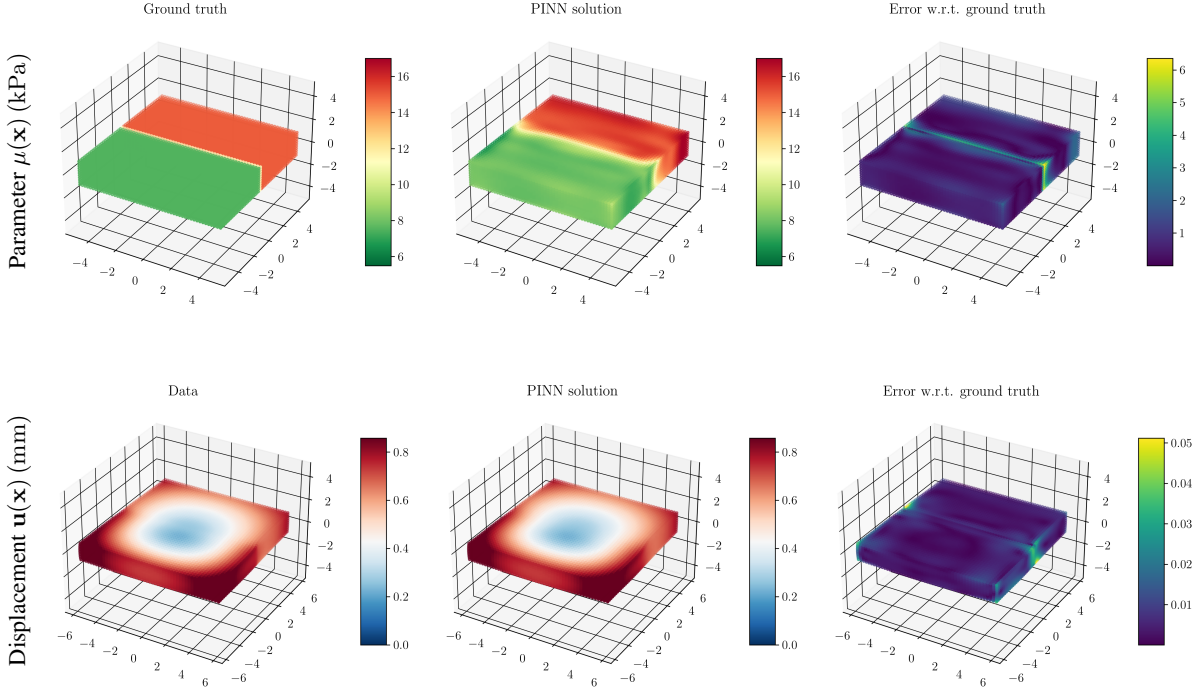


Figure 10: Isotropic heterogeneous material (two regions), SNR= 0.00. Estimation of parameter  $\mu(\mathbf{x})$  (top) and reconstruction of displacement  $\mathbf{u}(\mathbf{x})$  (bottom) by PINN using uncorrupted data and comparison with ground truth (absolute error).

Normalised $L^2$ - error of $\mu(\mathbf{x})$		
SNR	Res. 0.2 mm on data	Res. 0.4 mm on data
0.00	4.5e-2	4.8e-2
0.05	4.3e-2	4.9e-2
0.10	4.5e-2	4.7e-2

Table 5: Isotropic heterogeneous material (scar inclusion). Performance of the PINN in the estimation of the stiffness  $\mu(\mathbf{x})$  in presence of noisy measurement data with space resolution equal to 0.2 mm and 0.4 mm .

and training strategy allow us to consider a drastically lower number of neurons in the NN architecture, number of epochs and training points than in other works using PINNs for inverse problems in elasticity [27, 28], and this despite the fact that we consider nonlinear mechanics and a three-dimensional framework in this work. In this context, our preliminary results suggest the use of three fully connected hidden layers consisting of 32, 16, and 8 neurons for  $\text{NN}_{\mathbf{u}}$  (and three layers of 12, 8 and 4 neurons for  $\text{NN}_{\mu}$ , when  $\mu$  is treated as a field) being a good compromise between network representation capacity and computational costs, and the need to avoid overfitting. We have also considered rectangular architectures, composed of three hidden layers endowed with the same amount of neurons. However, this choice entailed higher computational costs — associated with the increased number of parameters to learn — and no noticeable improvement in terms of convergence properties of the method, as depicted in Section A.1. We have also studied the impact of the number of training points on the estimation of the stiffness field and reconstruction of the displacement field for one test case, as reported in Section A.2. We emphasise that, in the heterogeneous test cases, the displacement and stiffness reconstructed by the PINN differ from the ground truth, especially at the interfaces between regions with different properties. This is a well-known limitation of the PINNs, the *spectral bias* [44], which consists in the tendency of neural networks to learn low-frequency features. One way to mitigate this problem can be the use of Fourier feature embeddings [45], i.e. to pass input points through a Fourier feature mapping to let the PINN learn high-frequency functions. Preliminary results considering Fourier features for the test case with internal scar inclusion

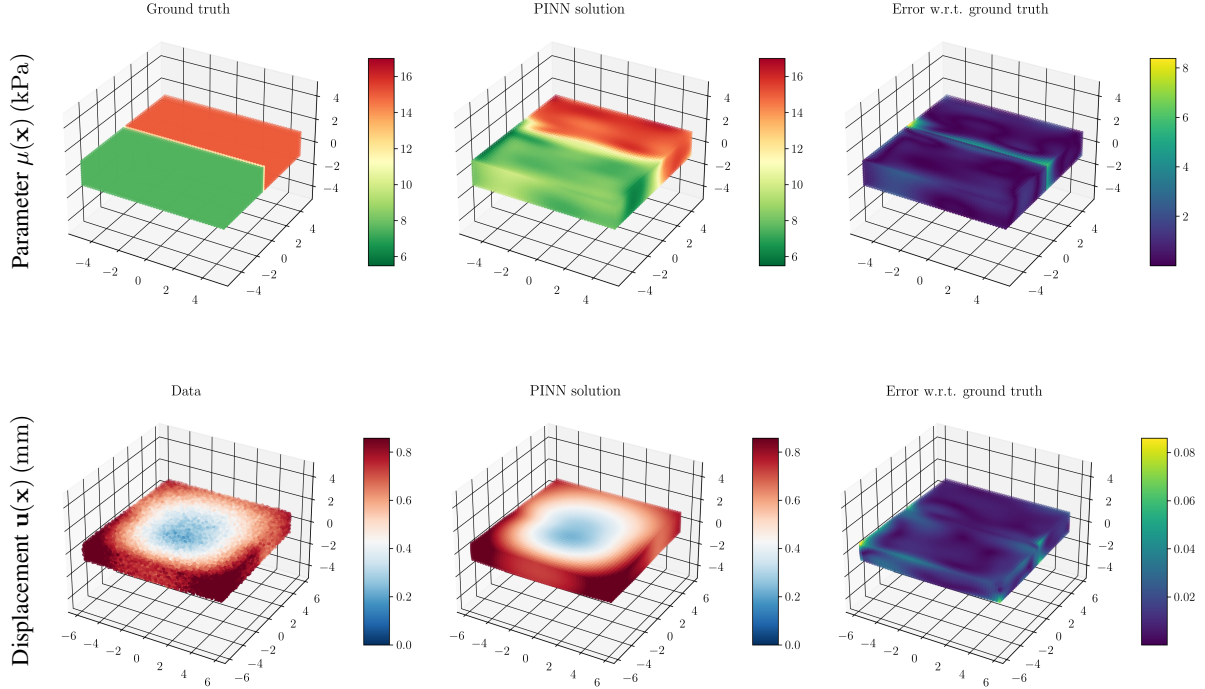


Figure 11: Isotropic heterogeneous material (two regions), SNR= 0.10. Estimation of parameter  $\mu(\mathbf{x})$  (top) and reconstruction of displacement  $\mathbf{u}(\mathbf{x})$  (bottom) by PINN using corrupted data and comparison with ground truth (absolute error).

are provided in Section B. However, they show a negligible improvement in the accuracy of predicted displacements  $\mathbf{u}$  and stiffness field  $\mu$  and more in-depth analysis is required to confirm these findings.

Note that the test cases represent a verification benchmark proving the properties of the proposed methodology. The ultimate goal is not only the estimation of homogeneous passive stiffness *per se*, as numerous, efficient methodologies have already been proposed for this aim [46–48], but also the evaluation of tissue heterogeneities and the non-invasive detection of scar regions. For this purpose, we envision several extensions and generalisations of the proposed method. First, we will consider more realistic and representative geometries, such as patient-specific computational domains retrieved by segmentation of clinical images. To deliver robust predictions on the reconstruction of the displacement and the estimation of the stiffness, we have considered several initialisations of the model with different random training (always generated from uniform random distribution), and we have shown the geometric mean and area spanned by the trajectories. However, more rigorous inverse uncertainty quantification is suitable in this context, s.a. the approach proposed in [49]. Another current limitation of the method is that we have not considered model uncertainties in the PINN estimation, these could be embedded as in [50] and will be considered in future investigations.

In this context, it is noteworthy to mention that the proposed methodology can also be used for the detection of solid tumors in soft tissues since strain maps are available f.e. in breast and liver imaging. Secondly, we aim at simultaneously reconstructing the passive stiffness and active contractility of the myocardium. To this end, we will consider a time-dependent counterpart of Equation (6) and an active stress approach, i.e. we will take into account a stress tensor  $\mathbf{P}$  that is the sum of a passive term, as discussed in this work, and an active term, e.g. the phenomenological law proposed in [51].

## 5 Conclusion

In this work we proposed a novel and robust methodology, based on physics-informed neural network techniques, to robustly reconstruct displacement fields and infer space-dependent passive material properties in soft tissue nonlinear biomechanical models from *in silico* data. Based on recent developments in scientific machine learning, the training of the NN is informed by the governing physics of the problem, which is included penalising the PDE (describing

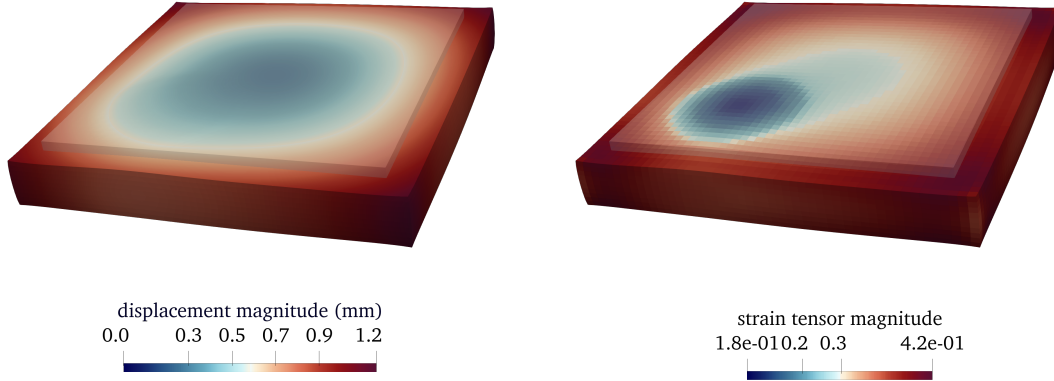


Figure 12: Isotropic test case with heterogeneous stiffness of Section 3.3.1, FEM solution Left: Displacement magnitude in mm. Right: strain magnitude. The rest configuration is superposed in shaded grey to the deformed configuration.

solid deformation) and respective boundary conditions in form of residual terms. The proposed methodology can estimate a space-dependent parameter solely based on a reduced number of displacement and, in some cases, strain data, dispensing from using stress data, which are not easily available in a realistic, clinical context. The predictions match the results of high-resolution finite element simulations in several test cases corresponding to healthy and pathological scenarios. We also showed that model inference is robust in presence of noise and we have tested different configurations of the NN, exploring the impact of training data and NN architecture on the predictions. This algorithm shows great potential for robust and effective identification of patient-specific, heterogeneous biophysical properties. This methodology contributes to the development of a personalised cardiovascular modelling approach leveraging cutting-edge mathematical and machine learning methodologies and has crucial clinical applications, e.g. to compute non-measurable biomarkers to support diagnosis and prediction of acute therapeutic responses and therapy planning.

## Acknowledgments

The authors acknowledge Dr. Matthias Gsell (Medical University of Graz, Austria) for his technical support with the 3D FEM biomechanical model. FEM simulations for this study were performed on the Vienna Scientific Cluster (VSC-4, VSC-5) under PRACE project #71962, which is maintained by the VSC Research Center in collaboration with the Information Technology Solutions of TU Wien. FC, FR and SP are members of the INdAM research group GNCS. EK acknowledges support from the BioTechMed-Graz Young Researcher Grant “CICLOPS — Computational Inference of Clinical Biomarkers from Non-Invasive Partial Data Sources”. This project has received funding from the ERA-NET co-fund action No. 680969 (ERA-CVD SICVALVES, JTC2019) funded by the Austrian Science Fund (FWF), Grant I 4652-B to CMA. This project has been partially supported by the INdAM GNCS Project 2023 CUP E53C22001930001. FR and SP acknowledge the support by the MUR, Italian Ministry of University and Research (Italy), grant Dipartimento di Eccellenza 2023-2027.

## Declarations

- Funding: FEM Simulations for this study were performed on the Vienna Scientific Cluster (VSC-4 and VSC-5), which is maintained by the VSC Research Center in collaboration with the Information Technology Solutions of TU Wien.
- Competing interests: The authors declare no competing interests.

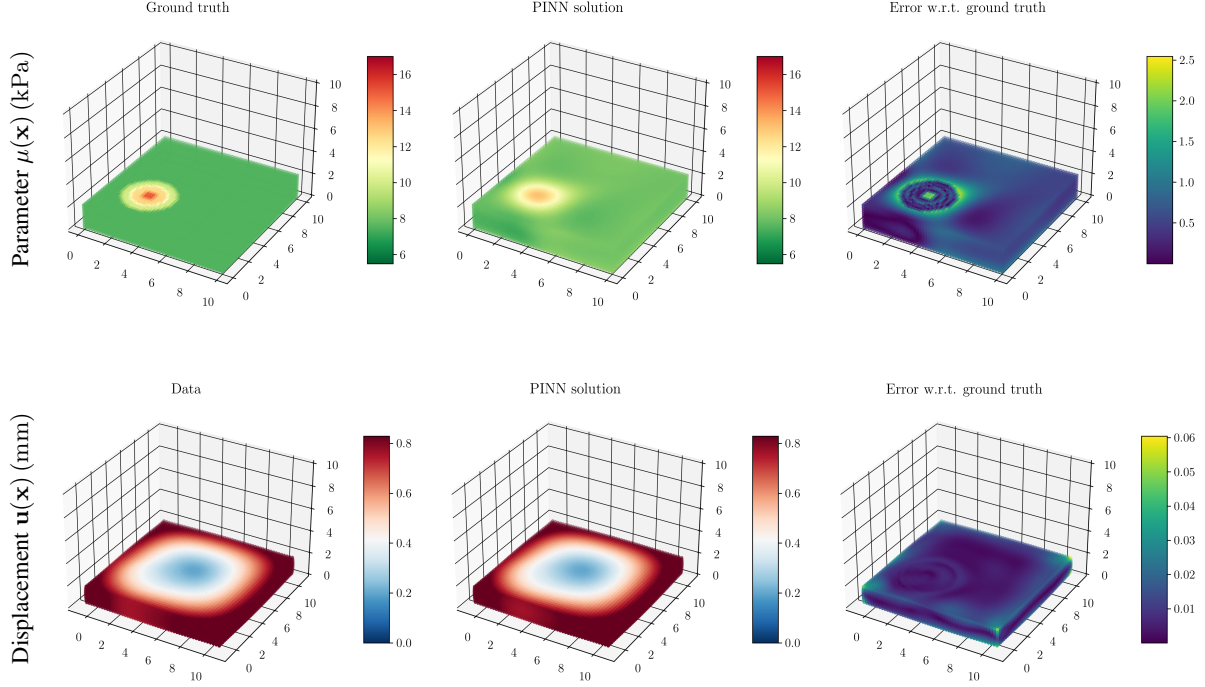


Figure 13: Isotropic material with scar inclusion, SNR= 0.00. Estimation of parameter  $\mu(\mathbf{x})$  (top) and reconstruction of displacement  $\mathbf{u}(\mathbf{x})$  (bottom) by PINN using uncorrupted data and comparison with ground truth (absolute error).

## Appendix A Sensitivity Analysis on model hyperparameters

For the sake of completeness, we have performed a comparison of the PINN predictions considering different NN architectures and number of training and collocation points used for training the PINN. For this purpose, we have restricted our analysis to the test case presented in Section 3.3.1, i.e. heterogeneous stiffness field with an internal scar inclusion.

### A.1 Neural Network Architecture

For this study, we have compared the results obtained with the proposed architecture (three layers with 32, 16, 8 neurons, respectively, for  $\text{NN}_{\mathbf{u}}$ , and 3 layers with 12, 8, 4 neurons, respectively, for  $\text{NN}_{\mu}$ ) with a common architecture for PINNs with the same number of neurons per layer. In particular, we have considered 3 layers with 32 neurons each for  $\text{NN}_{\mathbf{u}}$  and 3 layers with 12 neurons each for  $\text{NN}_{\mu}$ . The results depicted in Figure 18 and Table 6 show that the PINN estimation of the stiffness field  $\mu$ , as well as the reconstruction of the displacement field  $\mathbf{u}$ , are not improved considering a larger (and computationally more expensive) architecture, thus suggesting the use of the proposed NN architecture.

### A.2 Number of training and collocation points

For this analysis, we have considered three settings, respectively:

1.  $N_{\text{obs}} = 500$ ,  $N_{\text{pde}} = 2500$ ,  $N_{\text{bc}} = 50$  on  $\Gamma_{1,2,3,4}$ ,  $N_{\text{bc}} = 250$  on  $\Gamma_{5,6}$ ;
2.  $N_{\text{obs}} = 1000$ ,  $N_{\text{pde}} = 5000$ ,  $N_{\text{bc}} = 100$  on  $\Gamma_{1,2,3,4}$ ,  $N_{\text{bc}} = 500$  on  $\Gamma_{5,6}$ ;
3.  $N_{\text{obs}} = 2000$ ,  $N_{\text{pde}} = 10000$ ,  $N_{\text{bc}} = 200$  on  $\Gamma_{1,2,3,4}$ ,  $N_{\text{bc}} = 1000$  on  $\Gamma_{5,6}$ .

The second setting corresponds to the number of observation and collocation points used in this work. As shown in Figure 19 and Table 7, the first setting entails a slightly worse estimation of  $\mu(\mathbf{x})$  and a slightly worse reconstruction of  $\mathbf{u}(\mathbf{x})$  than the second setting. The third setting induces a comparable accuracy in the estimation of  $\mu(\mathbf{x})$  to the second setting and a slightly worse estimation of  $\mu(\mathbf{x})$  in case of higher SNR.

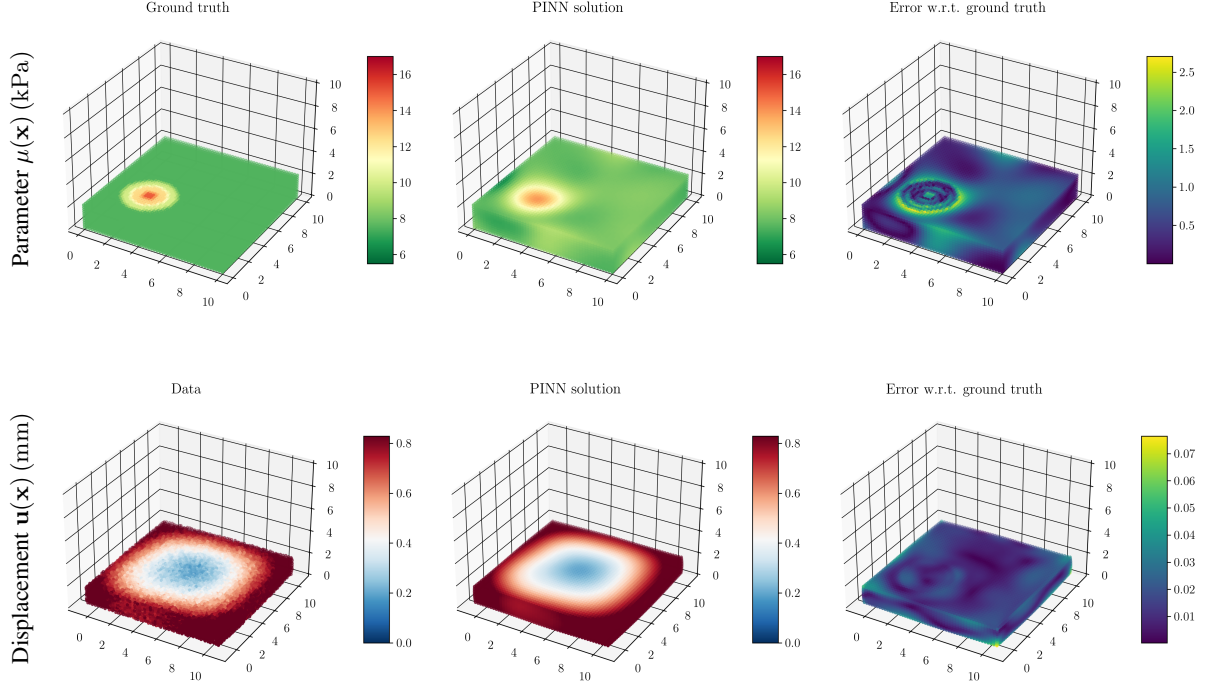


Figure 14: Isotropic material with scar inclusion, SNR= 0.10. Estimation of parameter  $\mu(\mathbf{x})$  (top) and reconstruction of displacement  $\mathbf{u}(\mathbf{x})$  (bottom) by PINN using corrupted data and comparison with ground truth (absolute error).

Normalised $L^2$ - error on $\mu(\mathbf{x})$		
SNR	Proposed architecture	Rectangular architecture
0.00	3.6e-3	3.0e-3
0.05	14.5e-3	14.3e-3
0.10	28.2e-3	28.3e-3
Normalised $L^2$ - error on $\mathbf{u}(\mathbf{x})$		
SNR	Proposed architecture	Rectangular architecture
0.00	4.5e-2	4.8e-2
0.05	4.3e-2	4.6e-2
0.10	4.5e-2	4.6e-2

Table 6: Isotropic heterogeneous material (scar inclusion). Performance of the PINN in the estimation of the stiffness  $\mu(\mathbf{x})$  in presence of noisy measurement data with original architecture ( $\text{NN}_{\mathbf{u}}$ : 3 layers with 32, 16, 8 neurons, respectively,  $\text{NN}_{\mu}$ : 3 layers with 12, 8, 4 neurons, respectively) and a rectangular architecture ( $\text{NN}_{\mathbf{u}}$ : 3 layers with 32 neurons each,  $\text{NN}_{\mu}$ : 3 layers with 12 neurons each).

## Appendix B Fourier feature embeddings

In order to explore potential improvements in the estimation of the stiffness field  $\mu(\mathbf{x})$  in case of heterogeneous material properties (e.g. in presence of a scar), we added Fourier Feature embeddings in the PINN learning algorithm, as proposed in [52]. This corresponds to add a Random features mapping  $\gamma$  as a coordinate embedding of the inputs, followed by the conventional fully-connected neural network used for PINNs. The random Fourier mapping  $\gamma$  is defined as (see [45] for more details):

$$\gamma(\mathbf{x}) = \begin{bmatrix} \cos(\mathbf{B}\mathbf{x}) \\ \sin(\mathbf{B}\mathbf{x}) \end{bmatrix} \quad (10)$$

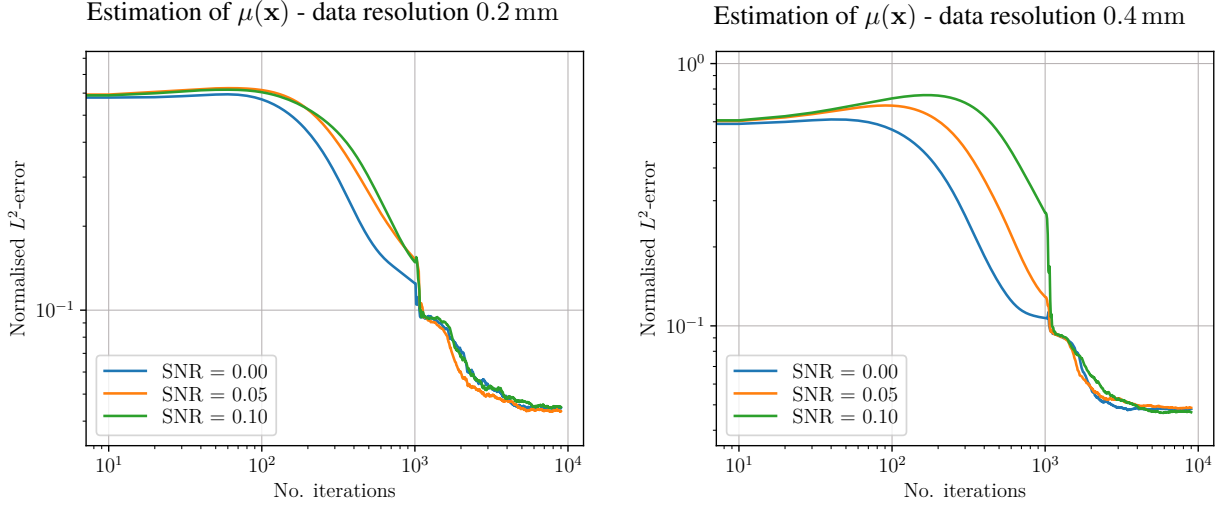


Figure 15: Isotropic heterogeneous material (scar inclusion). Normalised  $L^2$ -error for the estimation of the heterogeneous passive stiffness  $\mu(\mathbf{x})$  considering data corrupted by Gaussian white noise with different SNR. Prediction using displacement and strain data with resolution equal to 0.2 mm (left) and 0.4 mm (right). Results of five training processes. The solid line depicts the geometric mean; the shaded region is the area spanned by the trajectories.

Normalised $L^2$ - error on $\mu(\mathbf{x})$				Normalised $L^2$ - error on $\mathbf{u}(\mathbf{x})$			
SNR	Setting 1	Setting 2	Setting 3	SNR	Setting 1	Setting 2	Setting 3
0.00	4.3e-2	4.5e-2	4.7e-2	0.00	4.0e-3	3.6e-3	3.6e-3
0.05	4.6e-2	4.3e-2	4.4e-2	0.05	14.7e-3	14.5e-3	14.4e-3
0.10	4.5e-2	4.5e-2	4.3e-2	0.10	28.7 e-3	28.2e-3	28.0e-3

Table 7: Isotropic heterogeneous material (scar inclusion). Normalised  $L^2$ -error on the estimation of the stiffness  $\mu(\mathbf{x})$  and reconstruction of the displacement field  $\mathbf{u}(\mathbf{x})$  by PINNs in presence of noisy measurement data with different number of training and collocation points.

where each entry in  $\mathbf{B} \in \mathbb{R}^{m \times d}$  is sampled from a Gaussian distribution  $\mathcal{N}(0, \sigma_F^2)$  and  $\sigma_F$  is a user-defined hyper-parameter. In our preliminary study, we considered  $m = 16$  (in general, half of the number of neurons chosen in the first layer of the NN),  $d = 3$  (the dimension of the problem) and  $\sigma_F \in \{1, 2, 4\}$  (we considered  $\sigma_F \in [1, 10]$  as in [52]). As shown in Figure 20 and table 8, the inclusion of Fourier features embedding does not imply a noticeable improvement on the estimation of the stiffness field  $\mu(\mathbf{x})$ , and it has a slight effect on the reconstruction of the solution field  $\mathbf{u}$  (the PINN estimation of  $\mathbf{u}(\mathbf{x})$  and  $\mu(\mathbf{x})$  is more accurate for lower values of  $\sigma_F$ ).

## References

- [1] Steven A. Niederer, Michael S. Sacks, Mark Girolami, and Karen Willcox. Scaling digital twins from the artisanal to the industrial. *Nature Computational Science*, 1(5):313–320, May 2021. ISSN 2662-8457. doi:10.1038/s43588-021-00072-5. URL <http://dx.doi.org/10.1038/s43588-021-00072-5>.
- [2] Jorge Corral-Acero, Francesca Margara, Maciej Marciniak, Cristobal Rodero, et al. The ‘digital twin’ to enable the vision of precision cardiology. *European Heart Journal*, 41(48):4556–4564, March 2020. ISSN 1522-9645. doi:10.1093/eurheartj/ehaa159. URL <http://dx.doi.org/10.1093/eurheartj/ehaa159>.
- [3] Steven A. Niederer, Joost Lumens, and Natalia A. Trayanova. Computational models in cardiology. *Nature Reviews Cardiology*, 16(2):100–111, October 2018. ISSN 1759-5010. doi:10.1038/s41569-018-0104-y. URL <http://dx.doi.org/10.1038/s41569-018-0104-y>.
- [4] Radomir Chabiniok, Vicky Y. Wang, Myrianthi Hadjicharalambous, Liya Asner, et al. Multiphysics and multiscale modelling, data–model fusion and integration of organ physiology in the clinic: ventricular cardiac mechanics. *Interface Focus*, 6(2):20150083, April 2016. ISSN 2042-8901. doi:10.1098/rsfs.2015.0083. URL <http://dx.doi.org/10.1098/rsfs.2015.0083>.

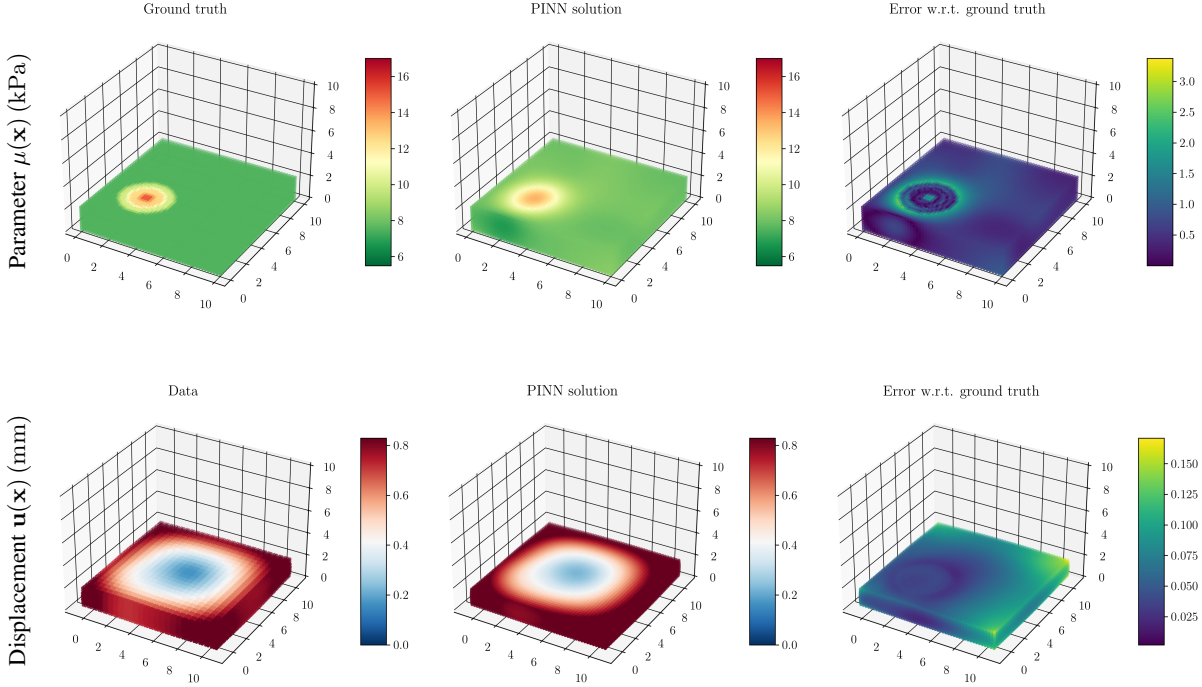


Figure 16: Isotropic material with scar inclusion, SNR= 0.00. Estimation of parameter  $\mu(\mathbf{x})$  (top) and reconstruction of displacement  $\mathbf{u}(\mathbf{x})$  (bottom) by PINN using uncorrupted data with lower resolution (0.4 mm) and comparison with ground truth (absolute error).

Normalised $L^2$ - error on $\mu(\mathbf{x})$			
SNR	$\sigma_F = 1$	$\sigma_F = 2$	$\sigma_F = 4$
0.00	4.8e-2	4.9e-2	5.0e-2
0.05	5.1e-2	5.1e-2	5.6e-2
0.10	5.7e-2	5.7e-2	6.5e-2
Normalised $L^2$ - error on $\mathbf{u}(\mathbf{x})$			
SNR	$\sigma_F = 1$	$\sigma_F = 2$	$\sigma_F = 4$
0.00	2.9e-3	3.0e-3	3.8e-3
0.05	14.4e-3	14.4e-3	14.5e-3
0.10	28.3e-3	28.3e-2	28.2e-3

Table 8: Isotropic heterogeneous material (scar inclusion). Normalised  $L^2$ -error on the estimation of the stiffness  $\mu(\mathbf{x})$  and reconstruction of the displacement field  $\mathbf{u}(\mathbf{x})$  by PINNs in presence of noisy measurement data and using Fourier features with different  $\sigma_F$ .

- [5] Alfio Quarteroni, Toni Lassila, Simone Rossi, and Ricardo Ruiz-Baier. Integrated heart–coupling multiscale and multiphysics models for the simulation of the cardiac function. *Computer Methods in Applied Mechanics and Engineering*, 314:345–407, February 2017. ISSN 0045-7825. doi:10.1016/j.cma.2016.05.031. URL <http://dx.doi.org/10.1016/j.cma.2016.05.031>.
- [6] Philippe Moireau and Dominique Chapelle. Reduced-order unscented kalman filtering with application to parameter identification in large-dimensional systems. *ESAIM: Control, Optimisation and Calculus of Variations*, 17(2):380–405, March 2010. ISSN 1262-3377. doi:10.1051/cocv/2010006. URL <http://dx.doi.org/10.1051/cocv/2010006>.

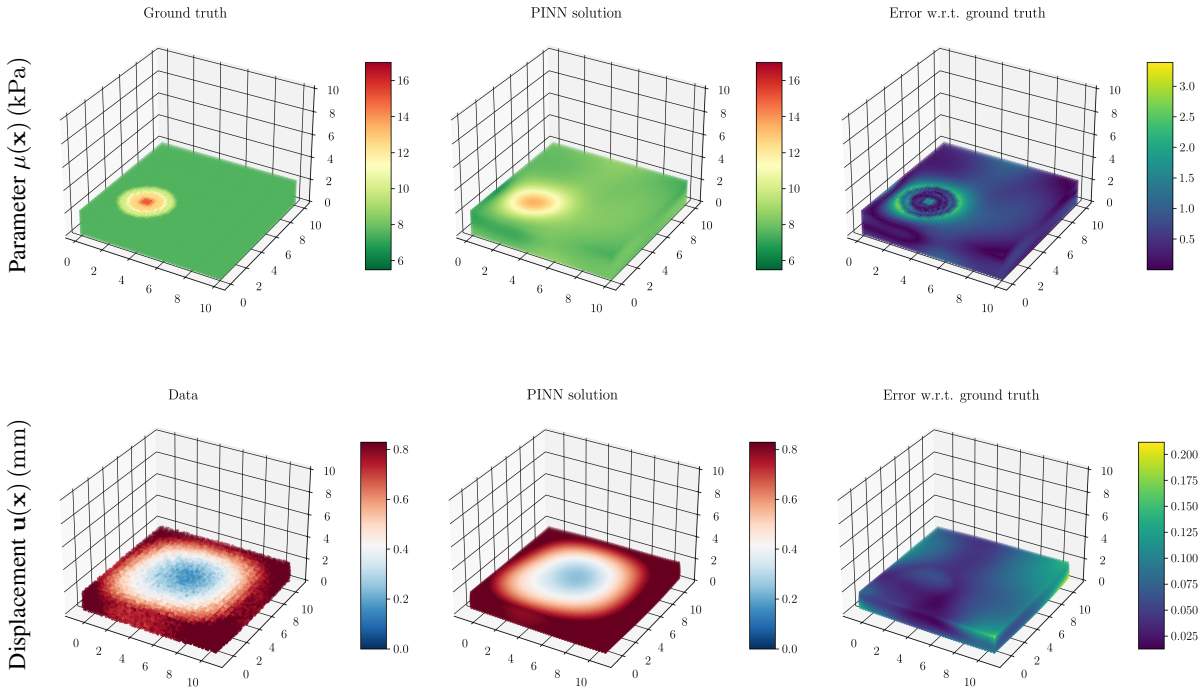


Figure 17: Isotropic material with scar inclusion, SNR= 0.10. Estimation of parameter  $\mu(\mathbf{x})$  (top) and reconstruction of displacement  $\mathbf{u}(\mathbf{x})$  (bottom) by PINN using corrupted data with lower resolution (0.4 mm) and comparison with ground truth (absolute error).

- [7] Jiahe Xi, Pablo Lamata, Jack Lee, Philippe Moireau, et al. Myocardial transversely isotropic material parameter estimation from in-silico measurements based on a reduced-order unscented kalman filter. *Journal of the Mechanical Behavior of Biomedical Materials*, 4(7):1090–1102, October 2011. ISSN 1751-6161. doi:10.1016/j.jmbbm.2011.03.018. URL <http://dx.doi.org/10.1016/j.jmbbm.2011.03.018>.
- [8] Cristóbal Bertoglio, Philippe Moireau, and Jean-Frederic Gerbeau. Sequential parameter estimation for fluid–structure problems: Application to hemodynamics. *International Journal for Numerical Methods in Biomedical Engineering*, 28(4):434–455, November 2011. ISSN 2040-7947. doi:10.1002/cnm.1476. URL <http://dx.doi.org/10.1002/cnm.1476>.
- [9] Alessandro Barone, Alessio Gizzi, Flavio Fenton, Simonetta Filippi, et al. Experimental validation of a variational data assimilation procedure for estimating space-dependent cardiac conductivities. *Computer Methods in Applied Mechanics and Engineering*, 358:112615, January 2020. ISSN 0045-7825. doi:10.1016/j.cma.2019.112615. URL <http://dx.doi.org/10.1016/j.cma.2019.112615>.
- [10] A. Caiazzo, Federica Caforio, Gino Montecinos, Lucas O. Muller, et al. Assessment of reduced-order unscented kalman filter for parameter identification in 1-dimensional blood flow models using experimental data. *International Journal for Numerical Methods in Biomedical Engineering*, 33(8), January 2017. ISSN 2040-7947. doi:10.1002/cnm.2843. URL <http://dx.doi.org/10.1002/cnm.2843>.
- [11] M. Sermesant, P. Moireau, O. Camara, J. Sainte-Marie, et al. Cardiac function estimation from mri using a heart model and data assimilation: Advances and difficulties. *Medical Image Analysis*, 10(4):642–656, August 2006. ISSN 1361-8415. doi:10.1016/j.media.2006.04.002. URL <http://dx.doi.org/10.1016/j.media.2006.04.002>.
- [12] Alexandre Imperiale, Dominique Chapelle, and Philippe Moireau. Sequential data assimilation for mechanical systems with complex image data: application to tagged-mri in cardiac mechanics. *Advanced Modeling and Simulation in Engineering Sciences*, 8(1), January 2021. ISSN 2213-7467. doi:10.1186/s40323-020-00179-w. URL <http://dx.doi.org/10.1186/s40323-020-00179-w>.
- [13] Mark Alber, Adrian Buganza Tepole, William R. Cannon, Suvarnu De, et al. Integrating machine learning and multiscale modeling—perspectives, challenges, and opportunities in the biological, biomedical, and behavioral

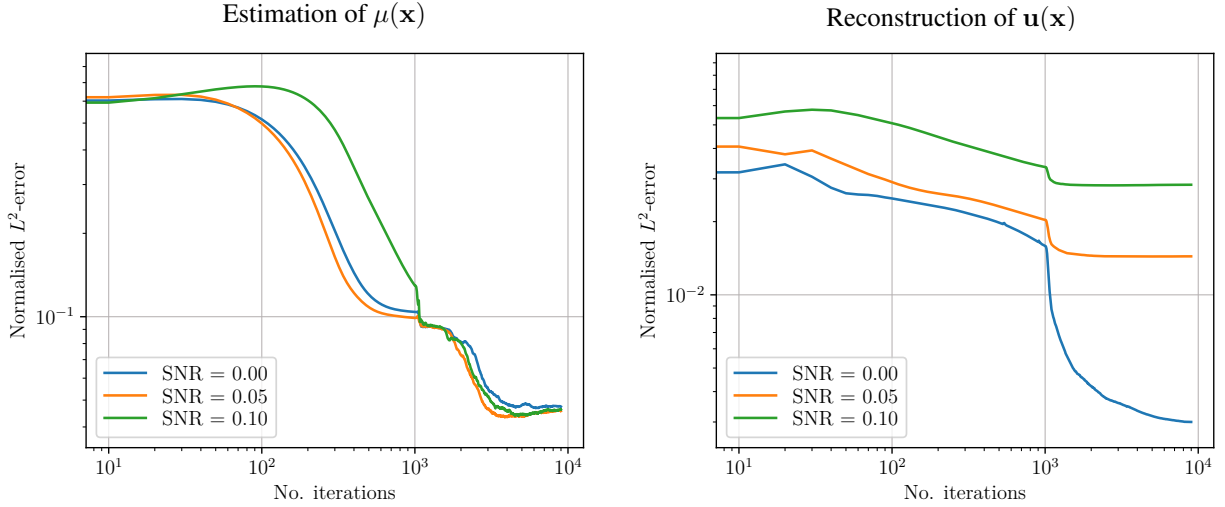


Figure 18: Isotropic heterogeneous material (scar inclusion). Normalised  $L^2$ -error on the estimation of the heterogeneous passive stiffness  $\mu(\mathbf{x})$  (left) and displacement field  $\mathbf{u}(\mathbf{x})$  (right) considering three layers of 32 neurons each (for  $\text{NN}_{\mathbf{u}}$ ) and three layers of 12 neurons each (for  $\text{NN}_{\mu}$ ). Results of 5 training processes. The solid line depicts the geometric mean; the shaded region is the area spanned by the trajectories.

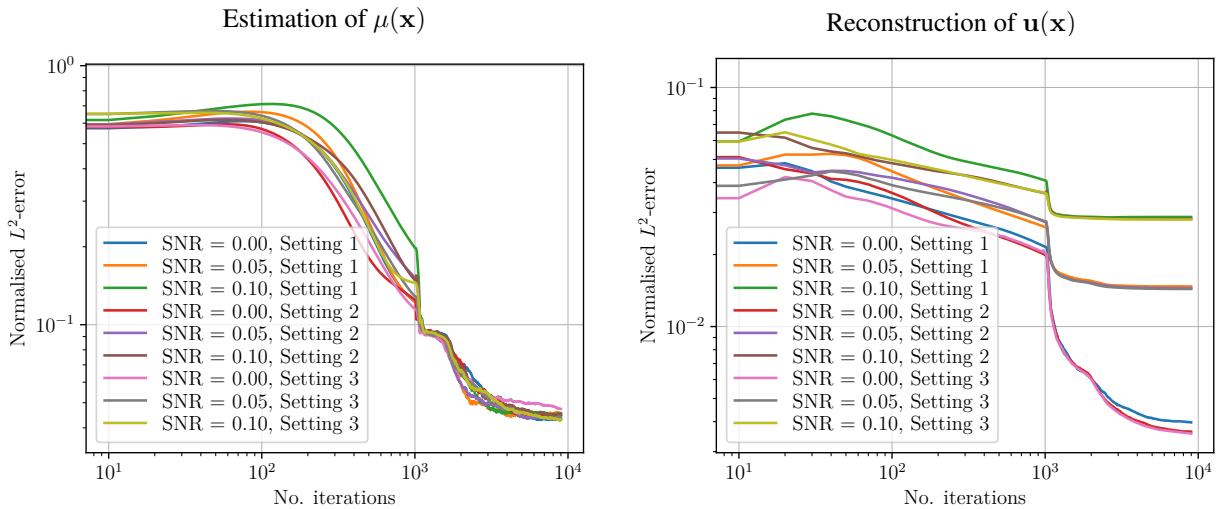


Figure 19: Isotropic heterogeneous material (scar inclusion). Normalised  $L^2$ -error on the estimation of the heterogeneous passive stiffness  $\mu(\mathbf{x})$  (left) and reconstruction of the displacement field  $\mathbf{u}(\mathbf{x})$  (right) considering noisy data with different SNR and different numbers of training and collocation points. Results of 5 training processes. The solid line depicts the geometric mean; the shaded region is the area spanned by the trajectories.

sciences. *npj Digital Medicine*, 2(1), November 2019. ISSN 2398-6352. doi:10.1038/s41746-019-0193-y. URL <http://dx.doi.org/10.1038/s41746-019-0193-y>.

- [14] Marlon Franke, Dominik K. Klein, Oliver Weeger, and Peter Betsch. Advanced discretization techniques for hyperelastic physics-augmented neural networks. *Computer Methods in Applied Mechanics and Engineering*, 416: 116333, November 2023. ISSN 0045-7825. doi:10.1016/j.cma.2023.116333. URL <http://dx.doi.org/10.1016/j.cma.2023.116333>.
- [15] Minliang Liu, Liang Liang, and Wei Sun. A generic physics-informed neural network-based constitutive model for soft biological tissues. *Computer Methods in Applied Mechanics and Engineering*, 372:113402, December 2020. ISSN 0045-7825. doi:10.1016/j.cma.2020.113402. URL <http://dx.doi.org/10.1016/j.cma.2020.113402>.

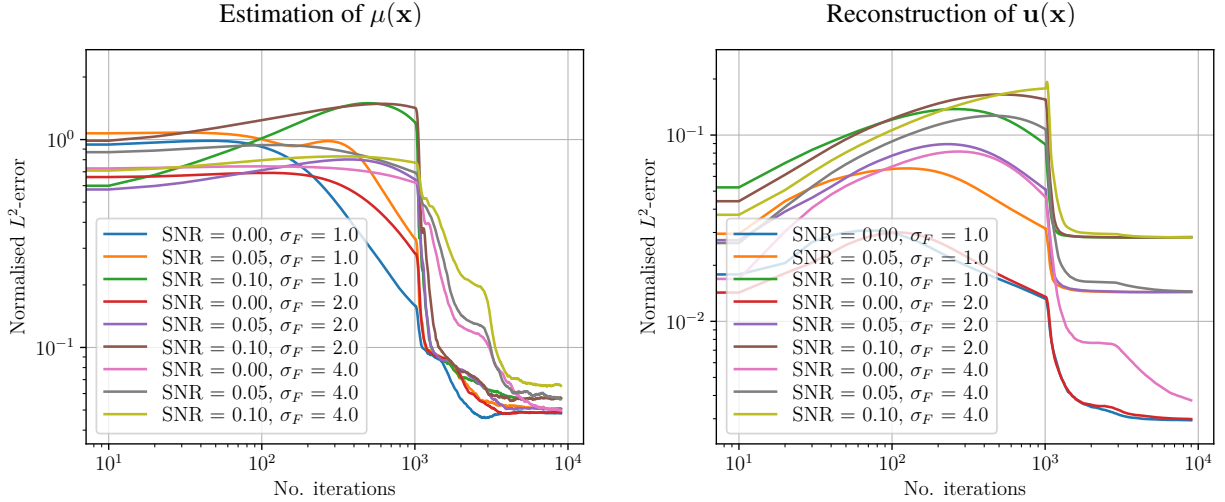


Figure 20: Isotropic heterogeneous material (scar inclusion). Normalised  $L^2$ -error on the estimation of the heterogeneous passive stiffness  $\mu(\mathbf{x})$  (left) and reconstruction of the displacement field  $\mathbf{u}(\mathbf{x})$  (right), considering data corrupted by Gaussian white noise with different SNR. PINN trained using Fourier features with different  $\sigma_F$ . Results of 5 training processes. The solid line depicts the geometric mean; the shaded region is the area spanned by the trajectories.

- [16] Liang Liang, Minliang Liu, John Elefteriades, and Wei Sun. Synergistic integration of deep neural networks and finite element method with applications for biomechanical analysis of human aorta. April 2023. doi:10.1101/2023.04.03.535423. URL <http://dx.doi.org/10.1101/2023.04.03.535423>.
- [17] M. Raissi, P. Perdikaris, and G.E. Karniadakis. Physics-informed neural networks: A deep learning framework for solving forward and inverse problems involving nonlinear partial differential equations. *Journal of Computational Physics*, 378:686–707, February 2019. ISSN 0021-9991. doi:10.1016/j.jcp.2018.10.045. URL <http://dx.doi.org/10.1016/j.jcp.2018.10.045>.
- [18] Salvatore Cuomo, Vincenzo Schiano Di Cola, Fabio Giampaolo, Gianluigi Rozza, et al. Scientific machine learning through physics-informed neural networks: Where we are and what’s next. *Journal of Scientific Computing*, 92(3), July 2022. ISSN 1573-7691. doi:10.1007/s10915-022-01939-z. URL <http://dx.doi.org/10.1007/s10915-022-01939-z>.
- [19] Atilim Gunes Baydin, Barak A. Pearlmutter, Alexey Andreyevich Radul, and Jeffrey Mark Siskind. Automatic differentiation in machine learning: a survey, 2018. Preprint at <https://arxiv.org/abs/1502.05767v4>.
- [20] Maziar Raissi, Alireza Yazdani, and George Em Karniadakis. Hidden fluid mechanics: Learning velocity and pressure fields from flow visualizations. *Science*, 367(6481):1026–1030, February 2020. ISSN 1095-9203. doi:10.1126/science.aaw4741. URL <http://dx.doi.org/10.1126/science.aaw4741>.
- [21] Minglang Yin, Xiaoning Zheng, Jay D. Humphrey, and George Em Karniadakis. Non-invasive inference of thrombus material properties with physics-informed neural networks. *Computer Methods in Applied Mechanics and Engineering*, 375:113603, March 2021. ISSN 0045-7825. doi:10.1016/j.cma.2020.113603. URL <http://dx.doi.org/10.1016/j.cma.2020.113603>.
- [22] Ehsan Haghghat, Maziar Raissi, Adrian Moure, Hector Gomez, et al. A deep learning framework for solution and discovery in solid mechanics, 2020. Preprint at <https://arxiv.org/abs/2003.02751>.
- [23] Carlos Ruiz Herrera, Thomas Grandits, Gernot Plank, Paris Perdikaris, et al. Physics-informed neural networks to learn cardiac fiber orientation from multiple electroanatomical maps. *Engineering with Computers*, 38(5):3957–3973, July 2022. ISSN 1435-5663. doi:10.1007/s00366-022-01709-3. URL <http://dx.doi.org/10.1007/s00366-022-01709-3>.
- [24] Thomas Grandits, Simone Pezzuto, Francisco Sahli Costabal, Paris Perdikaris, Thomas Pock, Gernot Plank, and Rolf Krause. Learning atrial fiber orientations and conductivity tensors from intracardiac maps using physics-informed neural networks. In Daniel B. Ennis, Luigi E. Perotti, and Vicky Y. Wang, editors, *Functional Imaging and Modeling of the Heart*, pages 650–658, Cham, 2021. Springer International Publishing. ISBN 978-3-030-78710-3. URL [https://doi.org/10.1007/978-3-030-78710-3\\_62](https://doi.org/10.1007/978-3-030-78710-3_62).

- [25] Carlos Ruiz Herrera, Thomas Grandits, Gernot Plank, Paris Perdikaris, Francisco Sahli Costabal, and Simone Pezzuto. Physics-informed neural networks to learn cardiac fiber orientation from multiple electroanatomical maps. *Engineering with Computers*, 38(5):3957–3973, 2022. doi:10.1007/s00366-022-01709-3. URL <https://doi.org/10.1007/s00366-022-01709-3>.
- [26] Bastian Zapf, Johannes Haubner, Miroslav Kuchta, Geir Ringstad, Per Kristian Eide, and Kent-Andre Mardal. Investigating molecular transport in the human brain from mri with physics-informed neural networks. *Scientific Reports*, 12(1):15475, 2022. doi:10.1038/s41598-022-19157-w. URL <https://doi.org/10.1038/s41598-022-19157-w>.
- [27] Ehsan Haghghat, Maziar Raissi, Adrian Moure, Hector Gomez, et al. A physics-informed deep learning framework for inversion and surrogate modeling in solid mechanics. *Computer Methods in Applied Mechanics and Engineering*, 379:113741, June 2021. ISSN 0045-7825. doi:10.1016/j.cma.2021.113741. URL <http://dx.doi.org/10.1016/j.cma.2021.113741>.
- [28] Ali Kamali, Mohammad Sarabian, and Kaveh Laksari. Elasticity imaging using physics-informed neural networks: Spatial discovery of elastic modulus and poisson’s ratio. *Acta Biomaterialia*, 155:400–409, January 2023. ISSN 1742-7061. doi:10.1016/j.actbio.2022.11.024. URL <http://dx.doi.org/10.1016/j.actbio.2022.11.024>.
- [29] Stefano Buoso, Thomas Joyce, and Sebastian Kozerke. Personalising left-ventricular biophysical models of the heart using parametric physics-informed neural networks. *Medical Image Analysis*, 71:102066, July 2021. ISSN 1361-8415. doi:10.1016/j.media.2021.102066. URL <http://dx.doi.org/10.1016/j.media.2021.102066>.
- [30] Christoph M. Augustin, Aurel Neic, Manfred Liebmann, Anton J. Prassl, et al. Anatomically accurate high resolution modeling of human whole heart electromechanics: A strongly scalable algebraic multigrid solver method for nonlinear deformation. *Journal of Computational Physics*, 305:622–646, January 2016. ISSN 0021-9991. doi:10.1016/j.jcp.2015.10.045. URL <http://dx.doi.org/10.1016/j.jcp.2015.10.045>.
- [31] Marina Strocchi, Matthias A.F. Gsell, Christoph M. Augustin, Orod Razeghi, et al. Simulating ventricular systolic motion in a four-chamber heart model with spatially varying robin boundary conditions to model the effect of the pericardium. *Journal of Biomechanics*, 101:109645, March 2020. ISSN 0021-9290. doi:10.1016/j.jbiomech.2020.109645. URL <http://dx.doi.org/10.1016/j.jbiomech.2020.109645>.
- [32] Francesco Regazzoni, Stefano Pagani, Alessandro Cosenza, Alessandro Lombardi, et al. A physics-informed multi-fidelity approach for the estimation of differential equations parameters in low-data or large-noise regimes. *Rendiconti Lincei - Matematica e Applicazioni*, 32(3):437–470, December 2021. ISSN 1120-6330. doi:10.4171/rlm/943. URL <http://dx.doi.org/10.4171/rlm/943>.
- [33] Diederik P. Kingma and Jimmy Ba. Adam: A method for stochastic optimization, 2017. Preprint at <https://arxiv.org/abs/1412.6980>.
- [34] R. Fletcher. *Practical Methods of Optimization*. Hoboken, May 2000. ISBN 9781118723203. doi:10.1002/9781118723203.
- [35] Martín Abadi, Ashish Agarwal, Paul Barham, Eugene Brevdo, et al. Tensorflow: Large-scale machine learning on heterogeneous distributed systems, 2015. URL <http://download.tensorflow.org/paper/whitepaper2015.pdf>.
- [36] Philippe G. Ciarlet. *Mathematical Elasticity: Three-Dimensional Elasticity*. Society for Industrial and Applied Mathematics, Philadelphia, January 2021. ISBN 9781611976786. doi:10.1137/1.9781611976786.
- [37] Federica Caforio, Christoph M. Augustin, Jordi Alastruey, Matthias A. F. Gsell, et al. A coupling strategy for a first 3d-1d model of the cardiovascular system to study the effects of pulse wave propagation on cardiac function. *Computational Mechanics*, 70(4):703–722, July 2022. ISSN 1432-0924. doi:10.1007/s00466-022-02206-6. URL <http://dx.doi.org/10.1007/s00466-022-02206-6>.
- [38] Elias Karabelas, Matthias A.F. Gsell, Gundolf Haase, Gernot Plank, et al. An accurate, robust, and efficient finite element framework with applications to anisotropic, nearly and fully incompressible elasticity. *Computer Methods in Applied Mechanics and Engineering*, 394:114887, May 2022. ISSN 0045-7825. doi:10.1016/j.cma.2022.114887. URL <http://dx.doi.org/10.1016/j.cma.2022.114887>.
- [39] Gerhard A. Holzapfel and Ray W. Ogden. Constitutive modelling of passive myocardium: a structurally based framework for material characterization. *Philosophical Transactions of the Royal Society A: Mathematical, Physical and Engineering Sciences*, 367(1902):3445–3475, September 2009. ISSN 1471-2962. doi:10.1098/rsta.2009.0091. URL <http://dx.doi.org/10.1098/rsta.2009.0091>.
- [40] P. J. Flory. Thermodynamic relations for high elastic materials. *Transactions of the Faraday Society*, 57:829, 1961. ISSN 0014-7672. doi:10.1039/TF9615700829. URL <http://dx.doi.org/10.1039/TF9615700829>.

- [41] Maziar Raissi, Alireza Yazdani, and George Em Karniadakis. Hidden fluid mechanics: Learning velocity and pressure fields from flow visualizations. *Science*, 367(6481):1026–1030, February 2020. ISSN 1095-9203. doi:10.1126/science.aaw4741. URL <http://dx.doi.org/10.1126/science.aaw4741>.
- [42] Ehsan Haghighat, Maziar Raissi, Adrian Moure, Hector Gomez, et al. A physics-informed deep learning framework for inversion and surrogate modeling in solid mechanics. *Computer Methods in Applied Mechanics and Engineering*, 379:113741, June 2021. ISSN 0045-7825. doi:10.1016/j.cma.2021.113741. URL <http://dx.doi.org/10.1016/j.cma.2021.113741>.
- [43] J. M. Guccione, A. D. McCulloch, and L. K. Waldman. Passive material properties of intact ventricular myocardium determined from a cylindrical model. *Journal of Biomechanical Engineering*, 113(1):42–55, February 1991. ISSN 1528-8951. doi:10.1115/1.2894084. URL <http://dx.doi.org/10.1115/1.2894084>.
- [44] Nasim Rahaman, Aristide Baratin, Devansh Arpit, Felix Draxler, et al. On the spectral bias of neural networks. In Kamalika Chaudhuri and Ruslan Salakhutdinov, editors, *Proceedings of the 36th International Conference on Machine Learning*, volume 97 of *Proceedings of Machine Learning Research*, pages 5301–5310, New York, 09–15 Jun 2019. Pmlr. URL <https://proceedings.mlr.press/v97/rahaman19a.html>.
- [45] Matthew Tancik, Pratul P. Srinivasan, Ben Mildenhall, Sara Fridovich-Keil, et al. Fourier features let networks learn high frequency functions in low dimensional domains, 2020. Preprint at <https://arxiv.org/abs/2006.10739>.
- [46] Laura Marx, Justyna A. Niestrawska, Matthias A.F. Gsell, Federica Caforio, et al. Robust and efficient fixed-point algorithm for the inverse elastostatic problem to identify myocardial passive material parameters and the unloaded reference configuration. *Journal of Computational Physics*, 463:111266, August 2022. ISSN 0021-9991. doi:10.1016/j.jcp.2022.111266. URL <http://dx.doi.org/10.1016/j.jcp.2022.111266>.
- [47] Henrik Finsberg, Ce Xi, Ju Le Tan, Liang Zhong, et al. Efficient estimation of personalized biventricular mechanical function employing gradient-based optimization. *International Journal for Numerical Methods in Biomedical Engineering*, 34(7), April 2018. ISSN 2040-7947. doi:10.1002/cnm.2982. URL <http://dx.doi.org/10.1002/cnm.2982>.
- [48] Kevin L. Sack, Eric Aliotta, Daniel B. Ennis, Jenny S. Choy, et al. Construction and validation of subject-specific biventricular finite-element models of healthy and failing swine hearts from high-resolution dt-mri. *Frontiers in Physiology*, 9, May 2018. ISSN 1664-042x. doi:10.3389/fphys.2018.00539. URL <http://dx.doi.org/10.3389/fphys.2018.00539>.
- [49] Liu Yang, Xuhui Meng, and George Em Karniadakis. B-pinns: Bayesian physics-informed neural networks for forward and inverse pde problems with noisy data. *Journal of Computational Physics*, 425:109913, January 2021. ISSN 0021-9991. doi:10.1016/j.jcp.2020.109913. URL <http://dx.doi.org/10.1016/j.jcp.2020.109913>.
- [50] Zongren Zou, Xuhui Meng, and George Em Karniadakis. Correcting model misspecification in physics-informed neural networks (pinns), 2023. Preprint at <https://arxiv.org/abs/2310.10776>.
- [51] Steven A. Niederer, Gernot Plank, Phani Chinchapatnam, Matthew Ginks, et al. Length-dependent tension in the failing heart and the efficacy of cardiac resynchronization therapy. *Cardiovascular Research*, 89(2):336–343, October 2010. ISSN 0008-6363. doi:10.1093/cvr/cvq318. URL <http://dx.doi.org/10.1093/cvr/cvq318>.
- [52] Sifan Wang, Hanwen Wang, and Paris Perdikaris. On the eigenvector bias of fourier feature networks: From regression to solving multi-scale pdes with physics-informed neural networks. *Computer Methods in Applied Mechanics and Engineering*, 384:113938, October 2021. ISSN 0045-7825. doi:10.1016/j.cma.2021.113938. URL <http://dx.doi.org/10.1016/j.cma.2021.113938>.